Inferring the Mean Effective Elastic Thickness of the Outer Ice Shell of Enceladus from Diurnal Crustal Deformation

Alexander Berne[1], Mark Simons[2], James Tuttle Keane[3], and Ryan S. Park[4]

[1]California Institute of Technology
[2]Caltech
[3]NASA Jet Propulsion Laboratory, California Institute of Technology
[4]Jet Propulsion Laboratory

December 16, 2022

Abstract

The thickness of the outer ice shell plays an important role in several geodynamical processes at ocean worlds. Here we show that observations of tidally-driven diurnal surface displacements can constrain the mean effective elastic thickness, del, of the ice shell. Such estimates are sensitive to any significant structural features that break spherical symmetry such as faults and lateral variation in ice shell thickness and structure. We develop a finite-element model of Enceladus to calculate diurnal tidal displacements for a range of del values in the presence of such structural heterogeneities. We find that the presence of variations in ice shell thickness can significantly amplify deformation in thinned regions. If major faults are also activated by tidal forcing—such as Tiger Stripes on Enceladus—their characteristic surface displacement patterns could easily be measured using modern geodetic methods. Within the family of Enceladus models explored, estimates of del that assume spherical symmetry a priori can deviate from the true value by as much as ˜ 20% when structural heterogeneities are present. Such uncertainty is smaller than that found with approaches that rely on static gravity and topography (˜ 250%) or analyzing diurnal libration amplitudes (˜ 25%) to infer del at Enceladus. As such, despite the impact of structural heterogeneities, we find that analysis of diurnal tidal deformation is a relatively robust approach to inferring del.

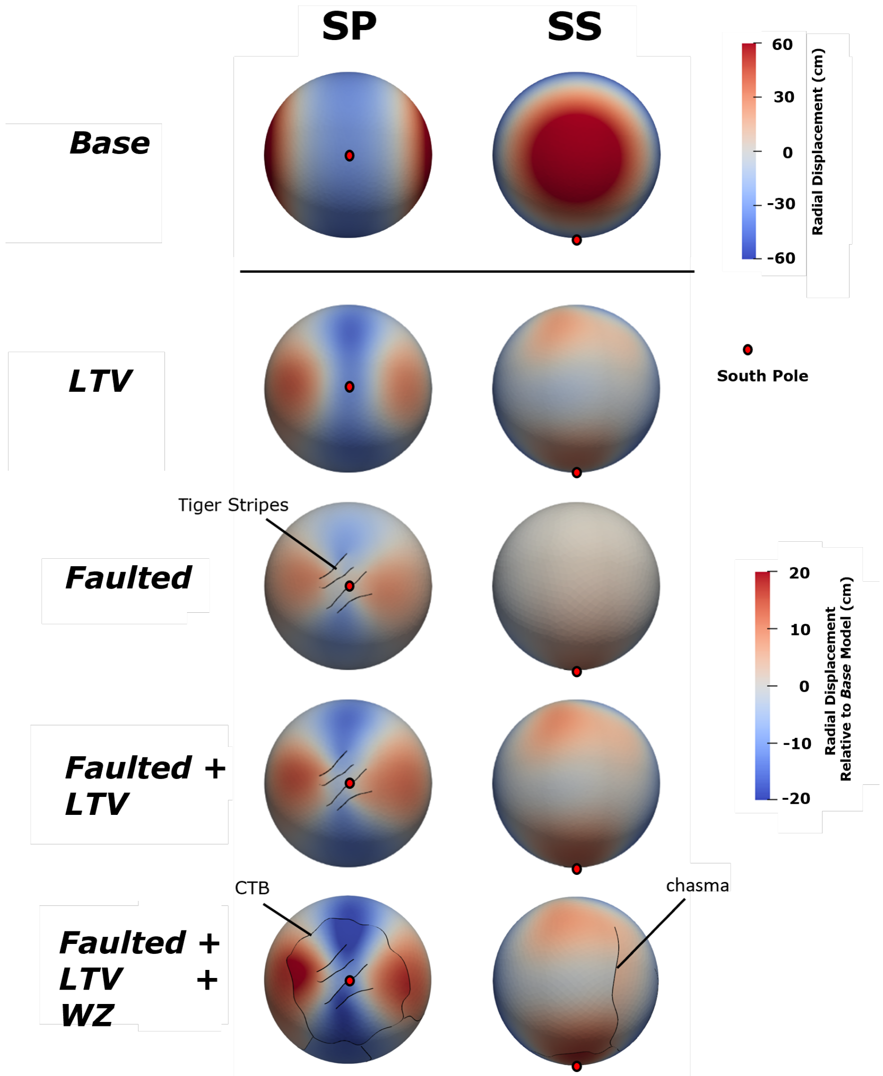
SP
SS
Base
LTV
Faulted
Faulted + LTV
Faulted + LTV + WZ
Tiger Stripes
CTB
chasma
60
30
0
-30
-60
Radial Displacement (cm)
South Pole
20
10
0
-10
-20
Radial Displacement Relative to Base Model (cm)

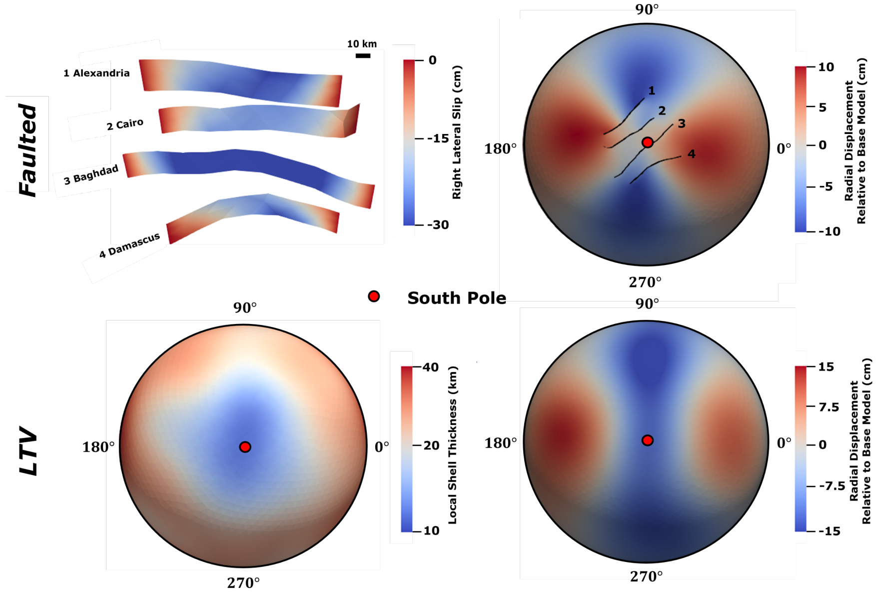
Faulted
LTV
1 Alexandria
2 Cairo
3 Baghdad
4 Damascus
10 km
Right Lateral Slip (cm)
Radial Displacement Relative to Base Model (cm)
Local Shell Thickness (km)
South Pole
90°
180°
0°
270°

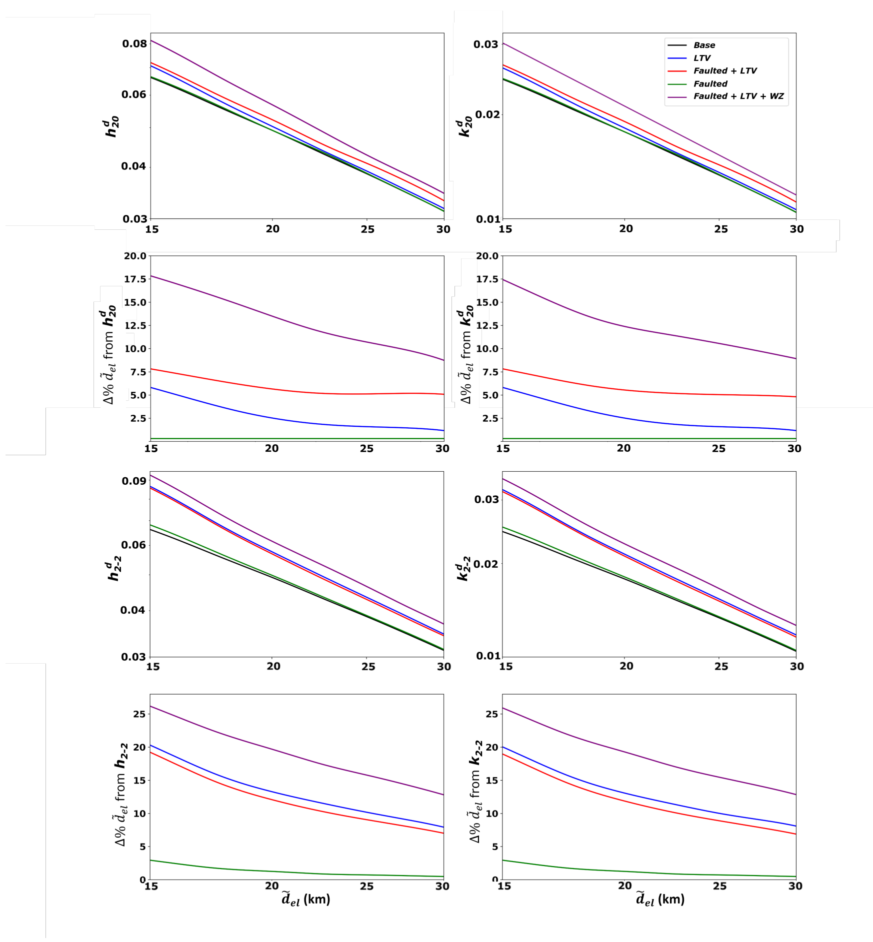
Base
LTV
Faulted + LTV
Faulted
Faulted + LTV + WZ
h^d_{20}
k^d_{20}
$\Delta\%\ \tilde{d}_{el}$ from h^d_{20}
$\Delta\%\ \tilde{d}_{el}$ from k^d_{20}
$h^d_{2\text{-}2}$
$k^d_{2\text{-}2}$
$\Delta\%\ \tilde{d}_{el}$ from $h_{2\text{-}2}$
$\Delta\%\ \tilde{d}_{el}$ from $k_{2\text{-}2}$
$\tilde{d}_{el}$ (km)

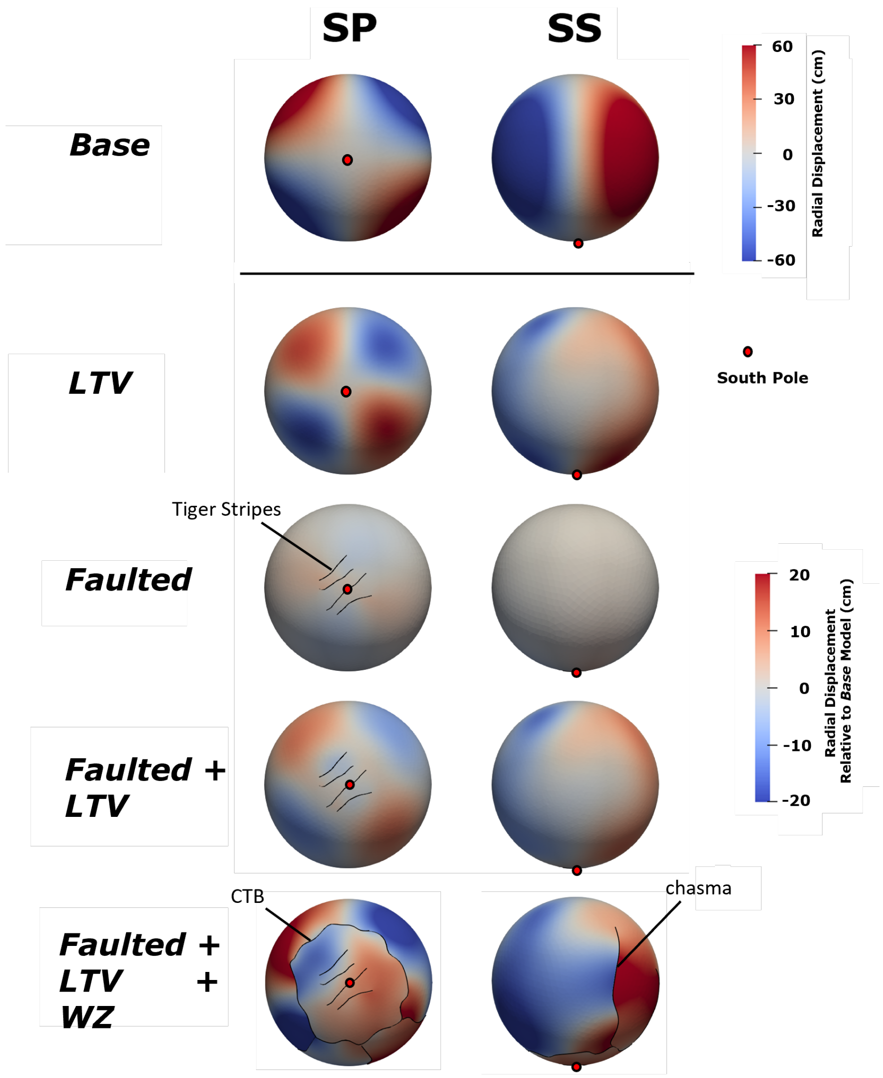
SP
SS
Radial Displacement (cm)
60
30
0
-30
-60
Base
LTV
South Pole
Tiger Stripes
Faulted
20
10
0
-10
-20
Radial Displacement Relative to Base Model (cm)
Faulted + LTV
CTB
chasma
Faulted + LTV + WZ

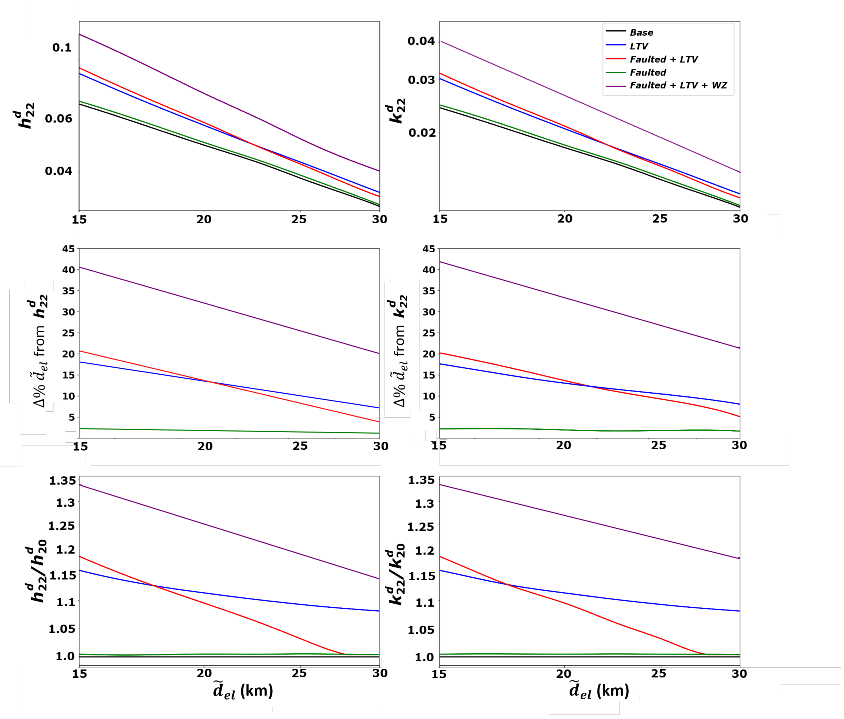
Base
LTV
Faulted + LTV
Faulted
Faulted + LTV + WZ
h_{22}^d
k_{22}^d
$\Delta\%\ \tilde{d}_{el}$ from h_{22}^d
$\Delta\%\ \tilde{d}_{el}$ from k_{22}^d
h_{22}^d/h_{20}^d
k_{22}^d/k_{20}^d
$\tilde{d}_{el}$ (km)

Inferring the Mean Effective Elastic Thickness of the Outer Ice Shell of Enceladus from Diurnal Crustal Deformation

Alexander Berne[1], Mark Simons[1], James Tuttle Keane[2], Ryan S. Park[2]

[1]California Institute of Technology, Pasadena, CA 91125 USA

[2]Jet Propulsion Laboratory, California Institute of Technology, Pasadena, CA 91109 USA

Key Points:

- Faults, crustal weak zones, and ice shell thickness variations affect how Enceladus responds to tidal forcing.
- Structural heterogeneities complicate inferring ice shell thickness using diurnal Love numbers.
- Measurements of tidal deformation at Enceladus would be a powerful probe of subsurface structure.

Corresponding author: Alexander Berne, `aberne@caltech.edu`

Abstract

The thickness of the outer ice shell plays an important role in several geodynamical processes at ocean worlds. Here we show that observations of tidally-driven diurnal surface displacements can constrain the mean effective elastic thickness, $\tilde{d}_{el}$, of the ice shell. Such estimates are sensitive to any significant structural features that break spherical symmetry such as faults and lateral variation in ice shell thickness and structure. We develop a finite-element model of Enceladus to calculate diurnal tidal displacements for a range of $\tilde{d}_{el}$ values in the presence of such structural heterogeneities. We find that the presence of variations in ice shell thickness can significantly amplify deformation in thinned regions. If major faults are also activated by tidal forcing—such as Tiger Stripes on Enceladus—their characteristic surface displacement patterns could easily be measured using modern geodetic methods. Within the family of Enceladus models explored, estimates of $\tilde{d}_{el}$ that assume spherical symmetry a priori can deviate from the true value by as much as $\sim 20\%$ when structural heterogeneities are present. Such uncertainty is smaller than that found with approaches that rely on static gravity and topography ($\sim 250\%$) or analyzing diurnal libration amplitudes ($\sim 25\%$) to infer $\tilde{d}_{el}$ at Enceladus. As such, despite the impact of structural heterogeneities, we find that analysis of diurnal tidal deformation is a relatively robust approach to inferring $\tilde{d}_{el}$.

Plain Language Summary

For ocean worlds such as Enceladus, it is useful to determine the thicknesses of the outer ice crust—as it determines the depth of the ocean, the thermal evolution of the body, and the rate at which material at the surface can be recycled to the ocean. Here we show that the mean effective elastic thickness of the ice crust can be inferred from measuring the deformation of the surface in response to tidal forces. We also demonstrate that the presence of large fault systems (such as the Tiger Stripes) or variations in the thickness of the ice crust affect Enceladus's response to tides.

1 Introduction

Enceladus, a moon orbiting Saturn approximately every 32.9 hrs, is demonstratively geologically active (Porco et al., 2006; Spencer et al., 2006; Hansen et al., 2006; Ingersoll et al., 2020). Erupting jets at the body's surface align with the position of four prominent, evenly spaced surface fractures (informally known as 'Tiger Stripes' (Porco et al., 2006)). These fractures produce jets or geysers that are the source of a water-ice-dominated plume emanating from the South Polar Terrain (SPT). The Tiger Stripes correlate with the position of anomalously high heat flux and regional thinning at the SPT (Spencer et al., 2006; Porco et al., 2014). Moreover, jet activity varies with orbital phase to produce maxima in plume brightness near orbital apoapse and periapse (Ingersoll et al., 2020). The correlation of period of plume brightness oscillation period and Enceladus's orbital period strongly suggests that diurnal tides regulate heat and mass transport in the outer ice shell (Hurford et al., 2007). We explore the interactions between crustal structure and diurnal deformation to improve our understanding of the interior dynamics of Enceladus.

Constraints on ice shell structure, in particular outer shell mean thickness $\tilde{d}_{ice}$, provide a first-order constraint on the thermal properties, interior structure, and potential for habitability of any ocean world. $\tilde{d}_{ice}$ is an essential parameter for understanding the total heat budget (Roberts & Nimmo, 2008), the potential for convection within the ice shell (Mitri & Showman, 2005), the radial extent of the core and ocean (Hemingway & Mittal, 2019), and the rate at which oxidized material cycles between the surface and the ocean (Zolotov & Shock, 2004). $\tilde{d}_{ice}$ also constrains plausible tidal heating mechanisms on Enceladus including viscous dissipation in the crust (Souček et al., 2019) and turbulent ocean flow (Hay & Matsuyama, 2019; Tyler, 2020).

Several approaches currently exist to infer $\tilde{d}_{ice}$. Static gravity and topography admittance modelling (Iess et al., 2014; McKinnon, 2015; Hemingway & Mittal, 2019; Akiba et al., 2022) and diurnal shell libration amplitude measurements (Thomas et al., 2016) yield estimates of $\tilde{d}_{ice}$ for Enceladus between 17–60 km ($\sim 250\%$) and 21–26 km ($\sim 25\%$) respectively. These methods rely on the presence of large-scale non-hydrostatic surface topography and a hydrostatic core, or alternatively, an orbital period comparable to the resonant frequency of the ice shell (less than a few days). Here, we explore an alternative approach that relies on the analysis of the response to short-period (i.e., diurnal) tidal forcing. Inferences of mean effective elastic thickness of the outer ice shell, $\tilde{d}_{el}$, from analysis of diurnal tides are relatively insensitive to assumptions regarding the core and are not contingent upon fortuitous structural or orbital conditions. The elastic behavior of ice is also largely insensitive to temperature (i.e., elastic moduli vary $< \pm 15\%$ across crustal temperatures $T = 70 - 273°$K; Shaw, 1985; Neumeier, 2018) and so inferences of $\tilde{d}_{el}$ from diurnal tides closely approximate estimates of $\tilde{d}_{ice}$ at Enceladus.

Differential gravitational attraction to a central, parent body (e.g., a planet) produces tides on orbiting satellites. Over timescales substantially greater than that of the orbital period (i.e., long-period), satellites deform as viscous fluids and the ultimate response to tidal forces is sensitive to radially varying internal density structure (e.g., Hubbard & Anderson, 1978). Bodies with eccentric orbits around their parent bodies experience an additional tidal force (i.e., the eccentricity or diurnal tide) which operates at a period equal to that of the orbit. At this timescale, any non-fluid interior layers may deform viscoelastically. For ocean-world bodies (i.e., where the outer ice shell and silicate core are mechanically decoupled by an intervening liquid ocean) deflection of the outer shell in response to diurnal tides is then relatively insensitive to the deep internal structure but is highly sensitive to $\tilde{d}_{el}$. Measurement of time-varying gravity or surface displacement can therefore be used to directly infer $\tilde{d}_{el}$.

The radial response of a body to time-dependent forcing can be described using gravitational and shape Love numbers k_l, h_l that depend on spherical harmonic degree l (Love, 1909). The $l = 2$ diurnal Love numbers k_2^d and h_2^d track the very long-wavelength elastic response of bodies to diurnal tides and are sensitive to long-wavelength elastic structure (i.e., $\tilde{d}_{el}$). We will demonstrate that there only exists a unique relationship between a body's response and a load at $l = 2$ for the limiting case of a fully spherically symmetric body. More generally, inferences of $\tilde{d}_{el}$ from diurnal Love numbers at Enceladus requires accounting for the potential impact of non-spherically symmetric structure.

For an arbitrary 3D structure, we can formulate a general linear relationship between spherical harmonics V_{lm} (i.e., of degree l and order m) of a driving gravitational potential $V(\bar{\Omega})$ which deforms (i.e., drives mass movement) within a body generating harmonics $U_{l'm'}$ of an induced gravitational potential potential $U(\bar{\Omega})$:

$$V(\bar{\Omega}) = \sum_{l=0}^{\infty} \sum_{m=-l}^{l} V_{lm} Y_{lm}(\bar{\Omega}) \tag{1a}$$

$$U(\bar{\Omega}) = \sum_{l'=0}^{\infty} \sum_{m'=-l'}^{l'} U_{l'm'} Y_{l'm'}(\bar{\Omega}) \tag{1b}$$

where $Y_{lm}(\bar{\Omega})$ denote real spherical harmonics, the prime ($'$) denotes induced components, and $\bar{\Omega}$ is the position variable comprising a co-latitude and longitude pair (θ, ϕ) (Note: we restrict our analysis to the induced gravitational response but could easily apply the methodology discussed in this section to derive the induced topographic response). For a linear elastic solid, deformation is linearly related to forcing (see also Supplementary S1.1). The tidal forcing harmonics V_{lm} accordingly map to harmonics $U_{l'm'}$ via linear Green's functions $\gamma_{lm}^{l'm'}$ which describe the elastic structure of a body:

$$\begin{bmatrix} U_{l'm'} \\ \vdots \\ \vdots \\ U_{\infty\infty} \end{bmatrix} = \begin{bmatrix} \gamma_{lm}^{l'm'} & \dots & \dots & \gamma_{\infty\infty}^{l'm'} \\ \vdots & \ddots & & \vdots \\ \vdots & & \ddots & \vdots \\ \gamma_{lm}^{\infty\infty} & \dots & \dots & \gamma_{\infty\infty}^{\infty\infty} \end{bmatrix} \begin{bmatrix} V_{lm} \\ \vdots \\ \vdots \\ V_{\infty\infty} \end{bmatrix} \tag{2}$$

Equation 2 demonstrates that $U_{l'm'}$ depends on both $\gamma_{lm}^{l'm'}$ and combinations of V_{lm}. In other words, the response of a body (i.e., at $l'm'$) will vary according to the changing shape of an applied load *despite* a fixed elastic structure. For diurnal tides, the driving potential is comprised of three harmonics V_{20}, V_{22}, and $V_{2\,\text{-}2}$ (Murray & Dermott, 1999) and Equation 2 simplifies to:

$$\begin{bmatrix} U_{l'm'} \\ \vdots \\ \vdots \\ U_{\infty\infty} \end{bmatrix} = \begin{bmatrix} \gamma_{20}^{l'm'} & \gamma_{22}^{l'm'} & \gamma_{2\,\text{-}2}^{l'm'} \\ \vdots & \vdots & \vdots \\ \vdots & \vdots & \vdots \\ \gamma_{20}^{\infty\infty} & \gamma_{20}^{\infty\infty} & \gamma_{2\,\text{-}2}^{\infty\infty} \end{bmatrix} \begin{bmatrix} V_{20} \\ V_{22} \\ V_{2\,\text{-}2} \end{bmatrix} \tag{3}$$

$U_{l\neq 2\, m} \neq 0$ indicate a coupling between forcing and response across spatial scales (i.e., 'mode coupling'; Dahlen & Tromp, 1998). To derive Love numbers, we restrict our analysis to the U_{20}, U_{22}, and $U_{2\,\text{-}2}$ components of the induced gravitational potential field. Equation 3 then simplifies to:

$$\begin{bmatrix} U_{20} \\ U_{22} \\ U_{2\,\text{-}2} \end{bmatrix} = \begin{bmatrix} \gamma_{20}^{20} & \gamma_{22}^{20} & \gamma_{2\,\text{-}2}^{20} \\ \gamma_{20}^{22} & \gamma_{22}^{22} & \gamma_{2\,\text{-}2}^{22} \\ \gamma_{20}^{2\,\text{-}2} & \gamma_{22}^{2\,\text{-}2} & \gamma_{2\,\text{-}2}^{2\,\text{-}2} \end{bmatrix} \begin{bmatrix} V_{20} \\ V_{22} \\ V_{2\,\text{-}2} \end{bmatrix} \tag{4}$$

The individual components $\gamma_{lm}^{l'm'}$ in Equation 4 contain information regarding the sphericity of a body's elastic structure. For a non-rigid body, diagonal components (i.e., $\gamma_{20}^{20}, \gamma_{22}^{22}, \gamma_{2\,\text{-}2}^{2\,\text{-}2}$) are always non-zero and are principally sensitive to bulk elastic properties (e.g., $\tilde{d}_{el}$; Wahr et al., 2006). Off-diagonal components (i.e., γ_{22}^{20}, γ_{20}^{22}, $\gamma_{2\text{-}2}^{22}$, $\gamma_{2\text{-}2}^{20}$, $\gamma_{22}^{2\text{-}2}$, $\gamma_{20}^{2\text{-}2}$) represent coupling between forcing and response at mutually distinct harmonics. At spatial wavelengths significantly greater than $\tilde{d}_{el}$, the outer ice crust of spherically symmetric ocean worlds conform to the shape of driving potential surfaces (i.e., following the thin-plate approximation originally derived from beam theory; Levinson, 1984). According to Equation 4, distinct diagonal components or non-zero off-diagonal components therefore imply the presence of non-spherically symmetric structure. For a spherically symmetric body, $\gamma_{22}^{20} = \gamma_{20}^{22} = \gamma_{2\,\text{-}2}^{22} = \gamma_{2\,\text{-}2}^{20} = \gamma_{22}^{2\,\text{-}2} = \gamma_{20}^{2\,\text{-}2} = 0$ and $\gamma_{20}^{20} = \gamma_{22}^{22} = \gamma_{2\,\text{-}2}^{2\,\text{-}2} = k_2^d$. Equation 4 then simplifies to:

$$\begin{bmatrix} U_{20} \\ U_{22} \\ U_{2\,\text{-}2} \end{bmatrix} = \begin{bmatrix} k_2^d & 0 & 0 \\ 0 & k_2^d & 0 \\ 0 & 0 & k_2^d \end{bmatrix} \begin{bmatrix} V_{20} \\ V_{22} \\ V_{2\,\text{-}2} \end{bmatrix} \tag{5}$$

We can define 'effective' Love numbers k_{2m}^d as quantities which track U_{2m} normalized by V_{2m} (i.e., $k_{2m} = U_{2m}/V_{2m}$) for an $l = 2$ driving potential with an arbitrary overall shape. According to Equation 5, a unique relationship between harmonics U_{2m} and V_{2m} exists only for spherically symmetric structures (i.e., $k_{2m} \to k_2$). More generally, k_{2m}^d are sensitive to non-spherically symmetric structure and the overall shape of the load (i.e., V_{20}, V_{22}, and $V_{2\,\text{-}2}$) such that $k_{20} \neq k_{22} \neq k_{2\,\text{-}2}$ (i.e., 'order splitting' or 'spectral leakage') (Behounkova et al., 2017; Ermakov et al., 2021; Vance et al., 2021). Several structures are expected to break spherical symmetry at Enceladus including lateral variations in thickness of the ice shell, structurally weak (e.g., highly fractured or damaged) zones, or the presence of major fault structures (Behounkova et al., 2017). We therefore expect that diurnal Love numbers are not directly sensitive to $\tilde{d}_{el}$ at Enceladus and inferences of $\tilde{d}_{el}$ from k_{2m}^d should account for the potential influence of structural heterogneities in the outer ice crust.

Several studies describe the relationship between elastic structure and diurnal deformation at Enceladus. Wahr et al., (2006) develop analytic expressions to calculate k_{2m}^d and h_{2m}^d from eccentricity tides at ocean worlds using an approach that only applies to spherically symmetric models. Beuthe (2018) extends this analysis of k_{2m}^d and h_{2m}^d to allow for variations in crustal thickness but assumes a thin-shelled approximation and does not include the potential impact of faults. The most sophisticated models to date by Souček et al., (2016), Behounkova et al., (2017), and Souček et al., (2019) simulate deformation using finite-element models (FEM) of the outer ice shell with both variations in ice thickness and weak zones. These studies do not specifically address the relationship between deformation and $\tilde{d}_{el}$ and exclude effects from a broader range of structural heterogeneities inferred from surface geology at Enceladus including large circum-tectonic boundaries and extensional fractures extending radially outward from the South Polar Terrain (i.e., chasma).

Here, we explore how estimates of $\tilde{d}_{el}$, based on analysis of diurnal tides, are potentially impacted by structural heterogeneities within the ice crust of Enceladus. We simulate deformation on tidally-loaded quasi-spherical shells using a FEM and compare results from five sets of end member models of Enceladus: (1) A spherically symmetric ice shell; (2) An ice shell with variations in thickness; (3) An ice shell with faults; (4) An ice shell with both variations in thickness and faults; and (5) An ice shell with faults, variations in thickness, and 'weak zones' (regions of reduced shear modulus) at locations corresponding to the position of additional structures inferred from Enceladus's geology (i.e., chasma and circum-tectonic boundaries). We parameterize the response of the shell by calculating k^d_{20}, k^d_{22}, $k^d_{2\text{-}2}$ and h^d_{20}, h^d_{22}, $h^d_{2\text{-}2}$, from deformed geometries and compare these predicted values with those predicted from models without structural heterogeneities. We then explore the challenge associated inferring $\tilde{d}_{el}$ from k^d_{20} and h^d_{20}, k^d_{22} and h^d_{22}, or h^d_{22} and $k^d_{2\text{-}2}$ posed by the presence of structural heterogeneities in the crust. We conclude by highlighting the potential for analyzing diurnal tides to determine $\tilde{d}_{el}$ both for Enceladus as well as for other ocean worlds.

2 Methods

We develop a quasi-spherical FEM of Enceladus that allows for structural heterogeneities in the ice shell and that can be used to predict the elastic response of the body to diurnal tidal loads. We first build an FEM mesh that reflects desired structural heterogeneities. We then use a modified version of the finite-element code Pylith (Aagaard et al., 2007) to calculate displacements on models subjected to tidal forcing. In post-processing, we extract $l = 2$ Love numbers from model displacements. We describe each of these steps in detail below.

2.1 Model Preparation

We consider five types of models that differ in the style of structural heterogeneity assumed: (1) a *Base* model without structural heterogeneities; (2) a model with large scale faults (a.k.a. *Faulted*); (3) a model with Lateral Thickness Variations (a.k.a. *LTV*);

(4) a combined model (a.k.a. *Faulted+LTV*); and (5) a combined model with additional weak zones at locations coincident with major geologic structures (a.k.a. *Faulted+LTV+WZ*). For each model, we develop a mesh with tetrahedral elements using the software package CUBIT (Skroch et al., 2019; CoreForm, 2020) and refine cell size in regions which locally exhibit high strain (e.g., near faults). We perform a mesh convergence test to verify our choice of element sizing parameters provide accurate Love number values on models with structural heterogeneities (see supplementary section S1.3).

- For the *Base* models, we mesh a spherical shell with a specified input thickness $\tilde{d}_{el}$. All of our models have baseline elastic parameters consistent with the rheology of ice (Jaccard, 1976; Shaw, 1985; Neumeier, 2018). We assign a base shear modulus value for ice of $G = 3.3$ GPa and a bulk modulus of $\mu = 8.6$ GPa (i.e., consistent with the formulation described in Souček et al., (2016) with $G = 3.3$ GPa and Poisson's ratio $\nu = 0.33$). For this analysis, we ignore viscous effects since viscous strain at the forcing period relevant for Enceladus (33 hours) is expected to be negligibly small (<0.1% of the total shell strain (Wahr et al., 2009), see also Supplemetary Section S1.2). Short-period elastic deformation of the core is also expected to be several orders of magnitude smaller than shell deformation (Schubert et al., 2007), thus we treat the core as a rigid body and ignore any impact deformation of the core may have on the response of the ice shell to eccentricity tides.

- For the *Faulted* models, we introduce fault surfaces that are through-going (i.e., they extend through the full thickness of the ice-shell) and are frictionless. Motion across these faults is restricted to shear with no opening. The explicit inclusion of fault surfaces within the FEM formulation uses a 'split-node' formulation whereby we duplicate nodes along the fault plane and introduce special cohesive cells between node sets (Melosh & Raefsky, 2009). Split-node formulations allow for robust calculations of fault-induced deformation and self-consistent predictions of fault slip. Our *Faulted* model specifically refers to a shell with four faults at the south pole consistent with the mapped extent of Tiger Stripes at Enceladus. We extract the surface trace of the Tiger Stripes from existing maps of Enceladus (Schenk, 2008).

- To construct the *LTV* models, we apply topography, H_{top}, to the outer surface of our base model geometry and modify the inner surface (i.e., the ice-ocean boundary), H_{bottom}, assuming isostatic (Airy) compensation. Given surface gravitational acceleration g_0, outer shell ice of density ρ_{ice}, ocean water of density ρ_w, gravitational acceleration at the ice-ocean interface g_{int}, mean radius of the ice-ocean boundary R_{int}, and mean radius of the outer surface R_0 (see Table 1 for chosen values of these parameters) (Hemingway & Matsuyama, 2017), we can write:

$$H_{bottom} = H_{top} \frac{\rho_{ice}}{(\rho_{ice} - \rho_w)} \frac{g_0}{g_{int}} \frac{R_0^2}{R_{int}^2} \tag{6}$$

Table 1. Assumed parameter values used in Equation 6. Parameter values taken from Schenk et al., (2018)

Parameter	**Value**	**Units**
ρ_{ice}	925	kg/m^3
ρ_w	1007	kg/m^3
g_0	0.113	m/s^2
g_{int}	0.120	m/s^2
R_0	252.1	km

Our *LTV* models use topography extracted from the shape model given by Nimmo et al. (2011) up to a maximum spherical harmonic degree $L_{max} = 8$. Our *Faulted+LTV* model includes both types of structural heterogeneities.

- Our *Faulted+LTV+WZ* models include additional through-going 'weak zones' at locations corresponding to the south polar circum-tectonic boundary, chasma, and Tiger Stripes. To generate weak zones, we assign material within 1-km wide zones to have an elastic shear modulus, G_{WZ}, reduced to $10^{-5}\,G$ (i.e., while maintaining a constant bulk modulus and ice density). By lowering the shear modulus, we approximate the behavior of damaged regions of the ice shell (i.e., as opposed to creating split-node surfaces for slipping fault structures). For these models, Tiger Stripes include both surrounding weak zone volumes and split-node surfaces along the fault plane. We extract chasma and circum-tectonic boundary positions from locations described by Yin & Pappalardo (2008).

2.2 Tidal Loading

For Enceladus, the driving potential produced by time-dependent eccentricity tides at a point $V(r, \theta, \phi)$ in an Enceladus-fixed frame (i.e., the ($\theta = 90°$, $\phi = 0°$) datum lies at the sub-Saturnian point, where θ is co-latitude and ϕ is longitude) is written as a combination of radial $V_{rad}(r, \theta, \phi)$ and librational $V_{lib}(r, \theta, \phi)$ terms (Murray & Dermott, 1999):

$$V_{rad}(r, \theta, \phi) = r^2 \omega^2 e \cdot \cos(\omega t) \, \frac{3}{4} \left(\mathrm{P}_{22}(\mu) \cos 2\phi - 2 \, \mathrm{P}_{20}(\mu)\right) \tag{7a}$$

$$V_{lib}(r, \theta, \phi) = r^2 \omega^2 e \cdot \sin(\omega t) \, \mathrm{P}_{22}(\mu) \sin 2\phi \tag{7b}$$

Each term in Equation 7 is scaled by the factor $\omega^2 e$, where $\omega = 5.307{*}10^{-5}$ s^{-1} is Enceladus's orbital angular velocity and $e = 0.0047$ is the body's orbital eccentricity. Time $t = 0, \frac{2\pi}{\omega}$ corresponds to orbital periapse. $P_{20}(\mu)$ and $P_{22}(\mu)$ are associated Legendre Functions with the nested function $\mu = \cos(\theta)$. We apply body forces, ocean tractions, topographic surface traction forces, and self-gravitational forces produced by the driving potential from Equation 7 and calculate displacement fields arising from these loads. We ignore inertial forces for our analysis (see Supplementary 1.1).

We use the 3D visco-elasto-plastic FEM code Pylith (Aagaard et al., 2008). Pylith is a well-established and extensively benchmarked tool developed in the terrestrial crustal dynamics community for studying tectonic processes on Earth. Pylith allows for complex bulk rheology, various formulations for fault behavior, and complex geometrical meshes. Pylith was originally designed for quasi-Cartesian problems; as such we have modified it to allow for modeling full spheres in a no-net-rotation/translation reference frame with central time-dependent body forces appropriate for eccentricity tides. We benchmark our tidal loading formulation as implemented in Pylith applied to our *Base* model against the program SatStress (Wahr et al., 2009) (see supplementary section S1.1-1.2).

2.3 Calculation of Love numbers

We post-process the resulting deformation fields to evaluate the $l = 2$ diurnal Love numbers, k^d_{20}, k^d_{22}, and $k^d_{2\text{-}2}$ or h^d_{20}, h^d_{22}, and $h^d_{2\text{-}2}$. The 'diurnal' Love numbers are distinct from 'fluid' Love numbers k^f_{20}, k^f_{22}, and $k^f_{2\text{-}2}$ or h^f_{20}, h^f_{22}, and $h^f_{2\text{-}2}$. 'Fluid' Love numbers are sensitive to the arrangement of a body's interior layers which deflect in response to long-period static tides in order to achieve hydrostatic equilibrium (Goldreich & Mitchell, 2010). By contrast, diurnal Love numbers depend on the elastic response of the body to short-period eccentricity tides (see Equation 7) and are superimposed onto the long-period tide. Moreover, diurnal Love numbers are usually at least an order of magnitude smaller than fluid Love numbers (Beuthe, 2018; Hemingway & Mittal, 2019). Relative to the fluid Love numbers, the diurnal Love numbers are less sensitive to deeper interior structure at ocean worlds (Wahr et al., 2009).

For h^d_{20}, h^d_{22}, and $h^d_{2\text{-}2}$ we expand the outer surface of our deformed geometry into spherical harmonics and separately compute the $l = 2$ zonal and sectoral coefficients H_{20}, H_{22}, and $H_{2\text{-}2}$. We calculate V_{20}, V_{22}, and $V_{2\text{-}2}$ using the $l = 2$ components of the tidal potential from Equation 7:

$$V_{20} = -\frac{3}{2}r^2\omega^2 e \cdot \cos(\omega t) \tag{8a}$$

$$V_{22} = \frac{3}{4}r^2\omega^2 e \cdot \cos(\omega t) \tag{8b}$$

$$V_{2\text{-}2} = r^2\omega^2 e \cdot \sin(\omega t) \tag{8c}$$

From V_{20}, V_{22}, $V_{2\text{-}2}$, h^d_{20}, h^d_{22}, and $h^d_{2\text{-}2}$ and the definition of the Love numbers, we have:

$$h^d_{20} = g_0 H_{20}/V_{20} \tag{9a}$$

$$h^d_{22} = g_0 H_{22}/V_{22} \tag{9b}$$

$$h^d_{2\text{-}2} = g_0 H_{2\text{-}2}/V_{2\text{-}2} \tag{9c}$$

Following a similar procedure for k^d_{20}, k^d_{22}, and $k^d_{2\text{-}2}$, we compute the $l = 2$ sectoral and zonal coefficients U_{20}, U_{22}, and $U_{2\text{-}2}$ of the spherical harmonic expansion of the induced gravitational potential field (see Equation 1) associated with the deformed geometry:

$$k^d_{20} = U_{20}/V_{20} \tag{10a}$$

$$k^d_{22} = U_{22}/V_{22} \tag{10b}$$

$$k^d_{2\text{-}2} = U_{2\text{-}2}/V_{2\text{-}2} \tag{10c}$$

As mentioned earlier, Love numbers defined in this way will depend on the time-varying shape and amplitude of the driving potential (i.e., see Equations 4 and 8). Thus, we expect values of k^d_{20}, k^d_{22}, and $k^d_{2\text{-}2}$ or h^d_{20}, h^d_{22}, and $h^d_{2\text{-}2}$ to vary over the tidal cycle at Enceladus. Since we aim to minimize the impact of non-spherically symmetric structure on inferences of $\tilde{d}_{el}$, we evaluate deformation at two unique points in the tidal cycle: $t =$

0 and $t = \frac{\pi}{2\omega}$. At $t = 0$ (or $\frac{\pi}{\omega}$), $V_{2\text{-}2} = 0$ (according to Equation 8) which eliminates the potential impact of the off-diagonal components $\gamma^{22}_{2\text{-}2}$, $\gamma^{20}_{2\text{-}2}$, $\gamma^{2\text{-}2}_{22}$, and $\gamma^{2\text{-}2}_{20}$ (from Equation 4) on values of k^d_{20} or k^d_{22}. Similarly, at $t = \frac{\pi}{2\omega}$ (or $\frac{3\pi}{2\omega}$), $V_{20} = V_{22} = 0$ which eliminates the impact of all off-diagonal components on values of $k^d_{2\text{-}2}$.

2.4 Previous FEM Models

Our FEMs are similar to, but distinct from, those described in the papers Souček et al., (2016) and Behounkova et al., (2017). We employ a tidal forcing formulation which is identical to that described in Souček et al., (2016) to generate body, ocean traction, and topographic loading forces. However, we include the effect of self-gravitation in our models (which modifies final calculated values of k^d_{20}, k^d_{22}, and $k^d_{2\text{-}2}$ or h^d_{20}, h^d_{22}, and $h^d_{2\text{-}2}$ by up to 3%). Souček et al., (2016) employ weak (i.e., highly damaged) zones as proxies the behavior of fault interfaces. In contrast, we adopt a split-node approach at the fault-plane to simulate deformation which enables straightforward calculations of fault slip. Souček et al., (2016) and Behounkova et al., (2017) also focus on the implications of deformation for tidal heating, while we focus here on the inference of shell structural parameters in the presence of structural heterogeneities. Finally, our models additionally consider the effect of fault zones beyond the Tiger Stripes and thereby identify the extent to which other major structural heterogeneities (e.g., chasma and circum-tectonic boundaries) may affect diurnal deformation patterns at Enceladus.

The most significant difference between models by Souček et al., (2016) and those described in this work relates to respective formulations for weak zones. Whereas Souček et al. (2016) reduce shear modulus to effectively negligible values while maintaining a constant Poisson's ratio within damaged regions, we formulate weak zones by locally reducing shear modulus and maintaining a constant bulk modulus. We choose to maintain a constant bulk modulus in weak zones since this formulation is consistent with the expected behavior of damaged ice permeated (or filled) by water (Kalyanaraman et al., 2020). (Note: we are able to largely reproduce the results of Souček et al., (2016) by employing weak zones only at Tiger Stripe locations and reducing both bulk and shear modulus to effectively negligible values, see Supplementary S1.2). Maintaining a constant bulk modulus allows weak zones to accommodate significant extensional and compressional strain and therefore substantially reduces displacements surrounding structural heterogeneities (e.g., the Tiger Stripes) relative to displacements from models by Souček et al., (2016) (See Figures 1 and Figure 2 in the Supplementary Documentation).

3 Results

Figures 1 and 2 show snapshots of the radial displacement fields from each of the five model classes. The upper panels show absolute displacements on our *Base* model whereas the subsequent panels show the radial displacement fields for models incorporating structural heterogeneities relative to our *Base* model. Not surprisingly, there is a substantial increase in localized deformation near zones of structural heterogeneities (i.e., consistent with model results from Souček et al., (2016) and Behounkova et al., (2017)). In the *LTV* model, the highest increases in displacement values occur near the South Pole where the ice shell is thinnest. In the *Faulted* model, radial displacements are maximum near fault tips (also at the South Pole) and follow a double-couple pattern characteristic of slip along these structures (e.g., Segall, 2010). We show example snapshots of fault slip along the Tiger Stripes evaluated on our *Faulted* model and crustal thickness variations in our *LTV* model in Figure 3. In our *Faulted+LTV+WZ* model, localized radial deformation is partitioned between the Tiger Stripes, chasma, and circum-tectonic boundaries in a complex manner with further increases in displacement near the Tiger Stripes due to extensional and shear strain localization along weak zones. Long-wavelength increases in displacement amplify values of the Love numbers for models incorporating structural heterogeneities. Moreover, surface deformation at this scale does not follow the pattern of the disturbing potential from Equation 7. This difference causes values of k^d_{20}, k^d_{22}, and $k^d_{2\text{-}2}$ (or h^d_{20}, h^d_{22}, and $h^d_{2\text{-}2}$) to diverge from each other (i.e., 'order-splitting').

Results for k^d_{20}, h^d_{20}, $k^d_{2\text{-}2}$. and $h^d_{2\text{-}2}$ from each model category are shown in Figure 4. Note that all the non-spherically symmetric models have enhanced values of k^d_{20}, h^d_{20}, $k^d_{2\text{-}2}$ and $h^d_{2\text{-}2}$ across all $\tilde{d}_{el}$ values consistent with the amplification of deformation shown in models with structural heterogeneities (see Figures 1 and 2). Figure 4 also shows the range of possible values of $\tilde{d}_{el}$ (i.e., $\Delta\%\tilde{d}_{el}$) corresponding to individual k^d_{20} and h^d_{20} or $k^d_{2\text{-}2}$. and $h^d_{2\text{-}2}$ values when treating *Base* and selected models with structural heterogeneities as end member scenarios. Results similar to those shown in Figure 4 illustrating the behavior of k^d_{22} and h^d_{22} are shown in Figure 5. Note the distinct values of k^d_{22} and h^d_{22} compared to k^d_{20} and h^d_{20} or $k^d_{2\text{-}2}$ and $h^d_{2\text{-}2}$ (i.e., 'order-splitting') in models with structural

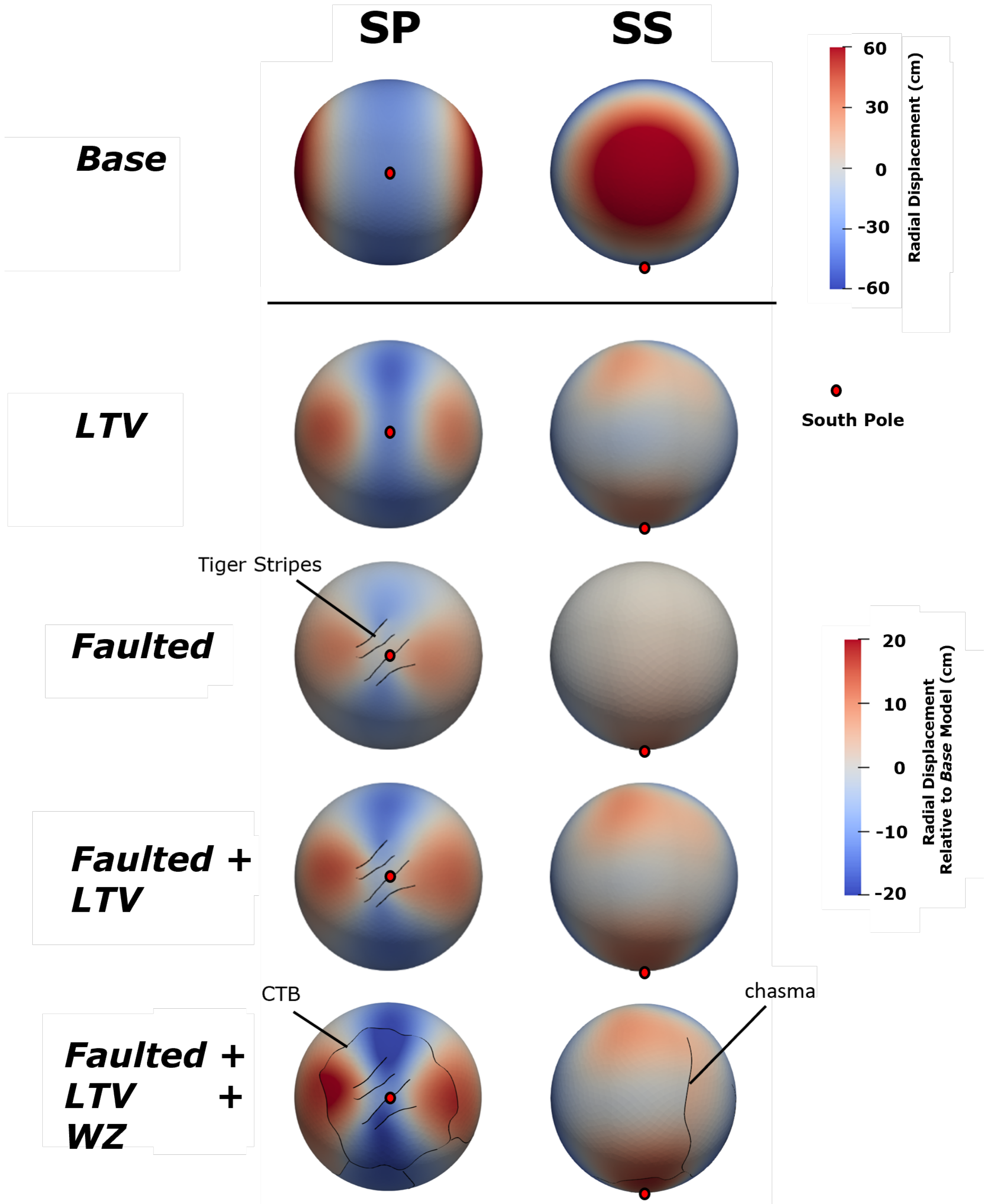

Figure 1. Snapshots of radial displacement from each model class viewed facing the south pole (SP, left column) and the sub-Saturnian point (SS, right column) evaluated at $t = 0$ (periapse). The top row shows the radial displacement in the *Base* model due to tidal forcing. The remaining rows present the differences in radial displacement between models with structural heterogeneities and the *Base* model. Each model shown assumes $\tilde{d}_{el} = 25$ km. Tiger Stripes, the south polar circum-tectonic boundary (CTB), and chasma are labelled. Figure 2 shows the same models at a different time in Enceladus's orbit.

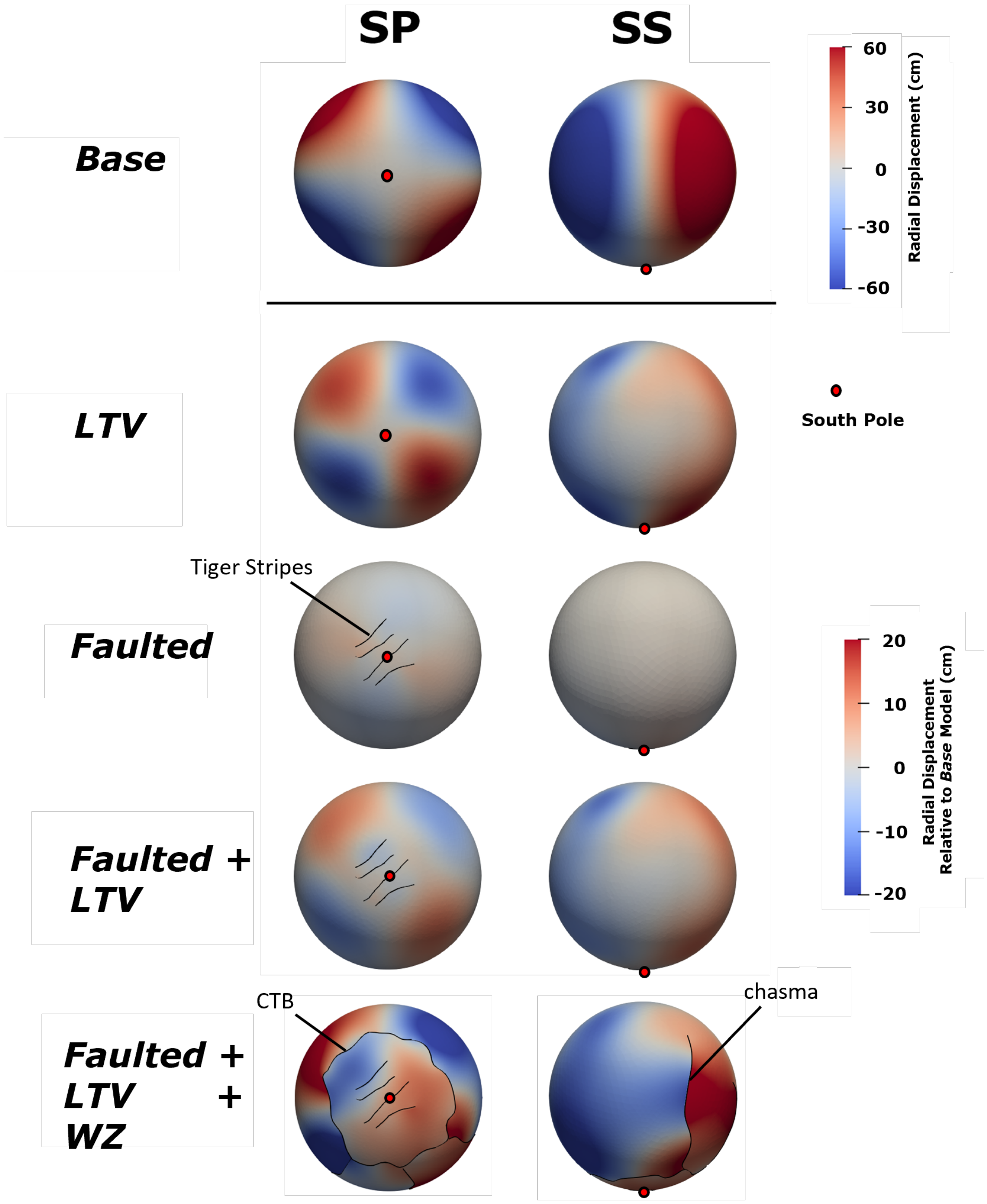

Figure 2. Snapshots of radial displacement from each model class viewed facing the south pole (SP, left column) and the sub-Saturnian point (SS, right column) evaluated at $t = \frac{\pi}{2\omega}$. The top row shows the radial displacement in the *Base* model due to tidal forcing. The remaining rows present the differences in radial displacement between models with structural heterogeneities and the *Base* model. Each model shown assumes $\tilde{d}_{el} = 25$ km. Tiger Stripes, the south polar circum-tectonic boundary (CTB), and chasma are labelled. Figure 1 shows the same models at a different time in Enceladus's orbit.

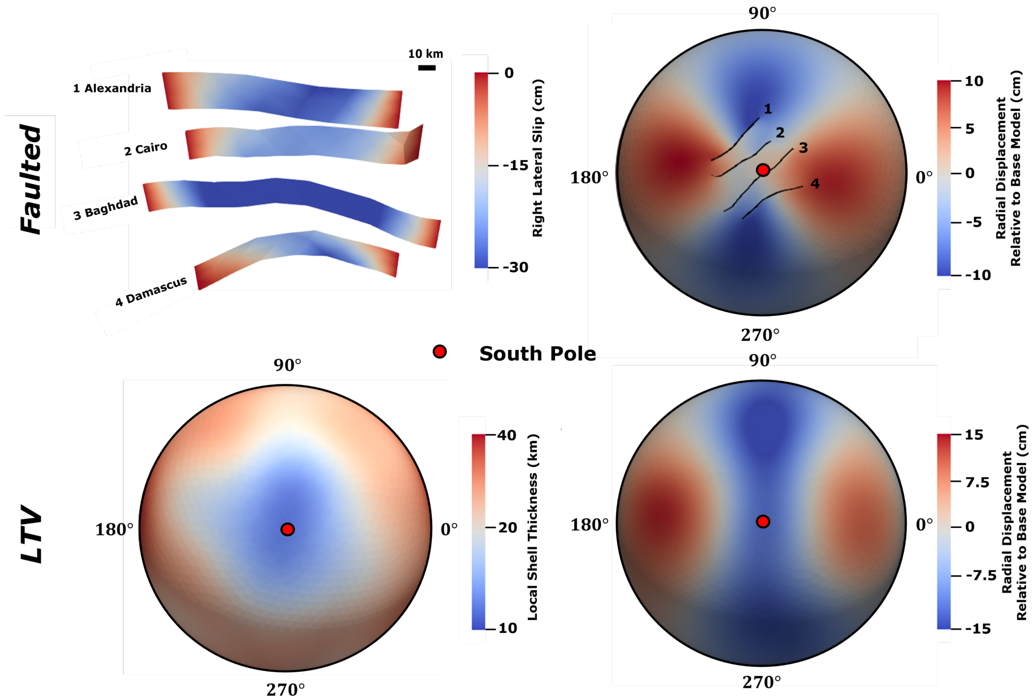

Figure 3. Snapshots of slip along the Tiger Stripes and regional thinning near the South Pole corresponding to deformation shown in *Faulted* (top row) and *LTV* (bottom row) models respectively in Figure 1. The upper left image shows a perspective view of fault slip on the Tiger Stripes, where negative (blue) values indicate left-lateral slip. The upper right shows a south polar projection (where 0° corresponds to the sub-Saturnian longitude), with fault locations overlaid on radial displacements (this is rescaled from the third row of Figure 1). The bottom row shows images of the crustal thickness variations (left) and a south polar projection showing radial displacements (right) evaluated from the *LTV* model (i.e., rescaled from the second row of Figure 1). Local thickness values are plotted in $\log_{10}$ scale. Each model shown assumes $\tilde{d}_{el} = 25$ km and is evaluated at $t = 0$ (periapse).

heterogeneities. To directly quantify the impact of structural heterogeneities on order-splitting, we additionally plot values of k^d_{22}/k^d_{20} and h^d_{22}/h^d_{20} vs. $\tilde{d}_{el}$ in Figure 5. We track k^d_{22}/k^d_{20} and h^d_{22}/h^d_{20} since these quantities implicitly account for the baseline impact of $\tilde{d}_{el}$ on Love numbers and are especially sensitive to the presence of structural heterogeneities near the South Pole of Enceladus (See discussion).

4 Discussion and Conclusion

We evaluate the relationship between mean effective elastic thickness, $\tilde{d}_{el}$, and diurnal Love numbers for a range of shell models with structural heterogeneities. We find that structural heterogeneities broaden the range of possible $\tilde{d}_{el}$ values corresponding to a measured Love number by about 41% in the most extreme case. The maximal range of plausible $\tilde{d}_{el}$ values increases less than 30% for $\tilde{d}_{el}$ values above 20 km (likely values of $\tilde{d}_{el}$ at Enceladus are between 21–26 km; Thomas et al., 2016). Moreover, if weak zones are not present on Enceladus then the range of plausible $\tilde{d}_{el}$ values further reduces to less than $\sim 20\%$.

The diurnal response of Enceladus to eccentricity tides is highly sensitive to variations in the thickness of the ice crust. *LTV* models show deviation in inferred $\tilde{d}_{el}$ values relative to *Base* models of up to 18%. The amplification of deformation in thinned regions (see Figures 1 and 3) is highly dependent on $\tilde{d}_{el}$. As $\tilde{d}_{el}$ approaches 15 km, effective elastic thickness approaches zero locally and strain increases rapidly near the South Pole. The resulting enhanced deformation drives the observed large increase in Love numbers at $\tilde{d}_{el} < 20$ km (Figure 4 and 5).

As implemented here, faults have less impact on long-wavelength deformation than do variations in the thickness of the ice crust. Fault structures in isolation bias inferred $\tilde{d}_{el}$ values from diurnal Love number values by up to 3%—rather insignificant. This observation follows from Figures 1 and 3 which shows that fault-induced deformation creates a strong double-couple deformation pattern as expected from slip on Tiger Stripes. Slip-induced deformation produces substantial radial displacement at scales comparable to the size of associated faults but reduced displacement at longer wavelengths. As such, for the Tiger Stripes along-fault slip only modestly increases diurnal Love number values. Moreover, we expect the influence of Tiger Stripe slip on diurnal love num-

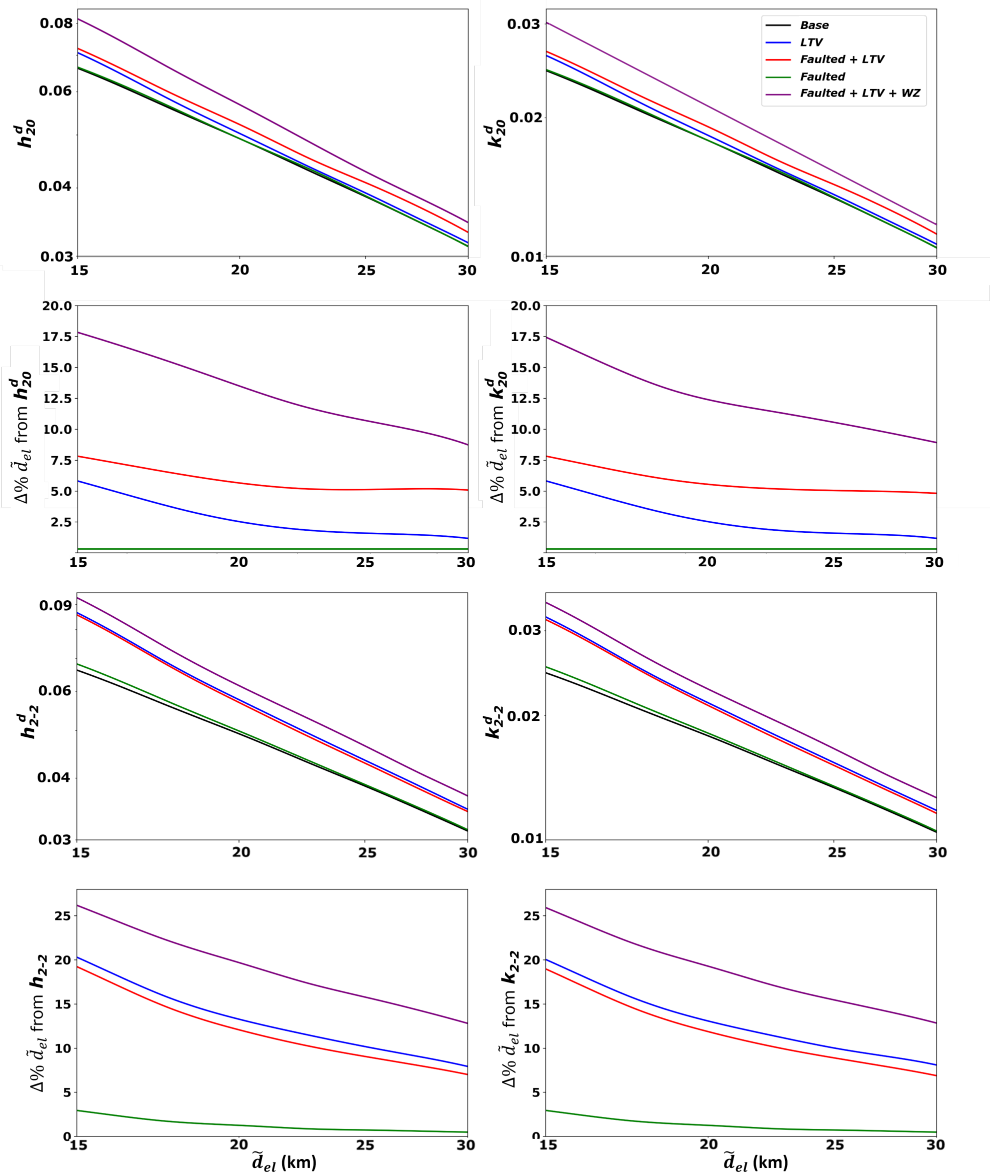

Figure 4. The relationship between deformation and mean effective elastic thickness, $\tilde{d}_{el}$. First row: h^d_{20} and k^d_{20} vs. $\tilde{d}_{el}$ for *Base* models (black lines), *LTV* models (blue lines), *Faulted* models (red lines), *Faulted+LTV* models (green lines), and *Faulted+LTV+WZ* (purple lines). We plot both axes in $\log_{10}$ scale and generate curves by evaluating h^d_{20} and k^d_{20} at t=0 (periapse) for 40 equally spaced $\tilde{d}_{el}$ values between 15 and 30 km. Second row: Percentage range of $\tilde{d}_{el}$ values corresponding to a fixed h^d_{20} and k^d_{20} value for each model category relative to the *Base* model. Curves in these plots are generated by evaluating the value of h^d_{20} and k^d_{20} corresponding to an $\tilde{d}_{el}$ in the *Base* model (i.e., $\tilde{d}_b$), identifying the $\tilde{d}_{el}$ value which maps to the same h^d_{20} and k^d_{20} values in models with structural heterogeneities (i.e., $\tilde{d}_{het}$) and evaluating $\Delta\%\ \tilde{d}_{el} = 100\cdot\frac{\tilde{d}_{het}-\tilde{d}_b}{\tilde{d}_b}\%$. X-axes are plotted in $\log_{10}$ scale. Third and Fourth Rows: similar to first and second rows (respectively) but for $h^d_{2\text{-}2}$ and $k^d_{2\text{-}2}$ evaluated at $t = \frac{\pi}{2\omega}$.

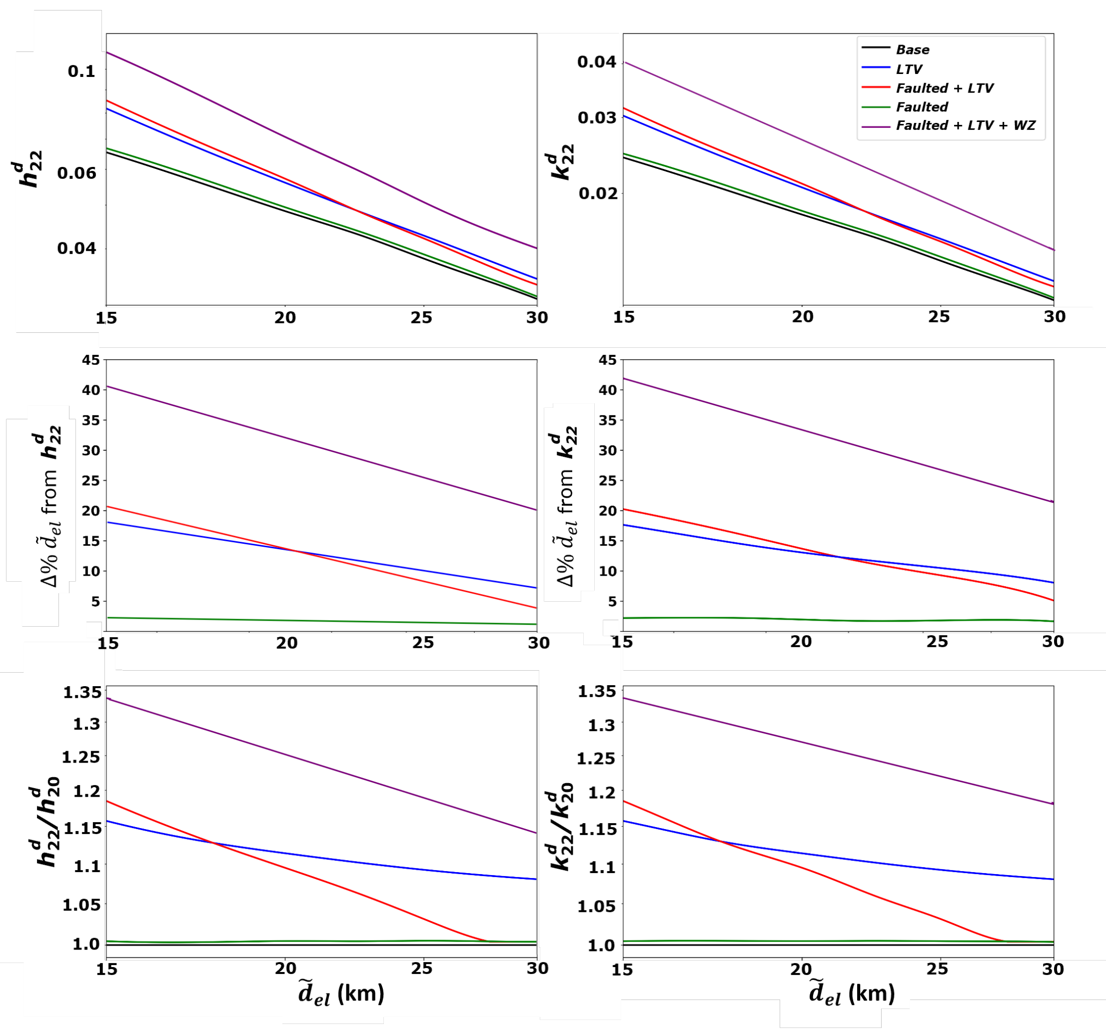

Figure 5. First row: Similar to first row of Figure 4 but for h^d_{22} and k^d_{22} instead of h^d_{20} and k^d_{20}. Second row: Similar to second row of Figure 4 for h^d_{22} and k^d_{22} instead of h^d_{20} and k^d_{20}. Third Row: 'order-splitting' associated with $l = 2$ Love numbers. We evaluate k^d_{20}, k^d_{22}, and $k^d_{2\text{-}2}$ or k^d_{20}, h^d_{22}, and $h^d_{2\text{-}2}$ at t=0 (periapse) for 40 equally spaced $\tilde{d}_{el}$ values between 15 and 30 km to compute k^d_{22}/k^d_{20} and h^d_{22}/h^d_{20}. X-axes are plotted in $\log_{10}$ scale.

ber values to decrease as maximum principal stresses rotate around the South Pole and fault slip decreases (see Figure 2).

Of the simplified structural heterogeneities considered, weak zones appear to have the most significant impact on the diurnal response of the ice shell to tides on Enceladus. The large spatial extent of the weak zones (i.e., 200–500 km in length or comparable to the radial length scale of Enceladus) and capacity to accommodate both additional normal- and shear-strain drives higher $\tilde{d}_{el}$ values than those produced from the presence of variations in the thickness of the crust and faults in isolation. We find that for cases with less pronounced weak zones (i.e., where $G_{WZ}/G > 10^{-5}$), the amplification of deformation drops dramatically (see Supplementary section S1.4 for details). These findings are consistent with results from Souček et al., (2016) and Behounkova et al., (2017) despite differences in the implementation of weak zones between the respective models (see section 2.4).

We find significant order-splitting (i.e., $k^d_{22}/k^d_{20} \neq 1$ and $h^d_{22}/h^d_{20} \neq 1$) in models with structural heterogeneities. Moreover, Figures 1 and 5 suggest k^d_{22}/k^d_{20} and h^d_{22}/h^d_{20} are highly sensitive to the scale of non-spherically symmetric structure near the South Pole. For *LTV* models, radial displacement patterns exhibit strong, long-wavelength quadrupole symmetry about the south pole (i.e., generating an $m = 2$ pattern) causing larger values of k^d_{22}/k^d_{20} and h^d_{22}/h^d_{20}. In contrast, slip along Tiger Stripe faults produces shorter-wavelength quadrupole deformation resulting in relatively smaller values of k^d_{22}/k^d_{20} and h^d_{22}/k^d_{20}. In *Faulted+LTV* models, slip-induced short wavelength deformation dominantly accommodates strain when $\tilde{d}$ >25 km (i.e., resulting in k^d_{22}/k^d_{20} values trending towards 1, whereas at smaller values of $\tilde{d}_{el}$, the effect of LTVs dominate such that k^d_{22}/k^d_{20} and $h^d_{22}/h^d_{20} >> 1$). Weak zones produce the highest levels of quasi-quadrupole deformation near the South Pole and so drive the largest values of k^d_{22}/k^d_{20} and h^d_{22}/h^d_{20}.

The predicted amplitude of tidally-driven radial surface displacements falls within a readily measurable range at Enceladus. According to Figures 1, 4, and 5 radial surface displacement exhibits a maximum amplitude of about 50–150 cm and differences in maximal radial displacement amplitudes between models are about 5–20 cm. These values are substantially larger than the sensitivity of Interferometric Synthetic Apreture Radar (InSAR) measurements of ground displacement (e.g., Simons & Rosen, 2015). Moreover, surface displacements of 5–20 cm can induce 2–80 μGal gravity anomalies which is greater than the expected detection limit of gravity measurements acquired from line-of-sight tracking between multiple orbiting spacecraft (e.g., Ramillien et al., 2004 and Dai et al., 2016). As such, a dedicated geodetic mission to Enceladus could be easily envisioned to make the measurements necessary for analysis of diurnal tides as discussed in this work.

We assume density structure for the crust and ocean (see Table 1), however the ocean density, ρ_w, is particularly uncertain. This uncertainty biases inferred values of $\tilde{d}_{el}$ derived from diurnal Love numbers since ρ_w scales the restoring force at the ice-ocean interface (see section 2.2 and supplementary S1.1). Uncertainties in estimates of ρ_w are approximately 5% (i.e., $\rho_w = 1000$–1050 kg/m^3; Čadek et al., 2016) and thus uncertainty in ρ_w can modify diurnal Love numbers by up to 4%. Propagated uncertainty from imprecise estimates of ρ_w is therefore slightly larger than model uncertainty associated with the presence of Tiger Stripes (3%) but substantially smaller than that produced from neglecting the potential influence of weak zones or variations in ice shell thickness. Moreover, changing the input value of ρ_w should not produce order-splitting and so does not alter inferences short-wavelength shell structure from comparisons of diurnal Love numbers.

While we have focused on the relationship between diurnal Love numbers and $\tilde{d}_{el}$ at Enceladus, a similar analysis could be done for Europa. In that case one should include the effect large-scale fault structures inferred from surface geology (e.g., Hoppa et al., 2000) but can exclude the effect of thickness variations due to the lack of significant non-hydrostatic topography (Nimmo et al., 2007). Ganymede, Callisto, and Titan do not exhibit large-scale crustal faulting and also apparently lack significant variations in outer ice shell thickness (McKinnon & Melosh, 1980; Cameron et al., 2019). As such, Enceladus appears to represent an extreme case where inferences of $\tilde{d}_{el}$ from diurnal Love numbers are most ambiguous. Nonetheless, we demonstrate that analysis of diurnal tides could serve as a useful tool for characterizing interior structure from future geodetic investigations at ocean worlds.

Open Research

This work utilizes the open-source finite element code Pylith (Aagaard et al., 2008) and the node-locked licensed software CUBIT (Skroch et al., 2019; CoreForm, 2020).

Acknowledgments

This research was supported by the Future Investigators in NASA Earth and Space Science and Technology (FINESST) Program. We also thank the Keck Institute for Space Studies (KISS) at California Institute of Technology for organizing two workshops about "Next-Generation Planetary Geodesy" which provided insight, expertise, and discussions that greatly assisted the research. We also thank Matthew Knepley, Brad Aagaard, and Charles Williams for providing invaluable advice to modify Pylith for the simulations described this work. A portion of this research was supported by a Strategic Research and Technology Development task led by James T. Keane and Ryan S. Park at the Jet Propulsion Laboratory, California Institute of Technology, under a contract with the National Aeronautics and Space Administration (80NM0018D0004).

References

Aagaard, B., Williams, C., & Knepley, M. (2007). PyLith: A Finite-Element Code for Modeling Quasi-Static and Dynamic Crustal Deformation. *Eos*, *88(52)*.

Akiba, R., Ermakov, A. I., & Militzer, B. (2022). Probing the icy shell structure of ocean worlds with gravity–topography admittance. *The Planetary Science Journal*, *3*. doi: 10.3847/psj/ac4d2b

Behounkova, M., Soucek, O., Hron, J., & Cadec, O. (2017). Plume activity and tidal deformation on enceladus influenced by faults and variable ice shell thickness. *Astrobiology*, *17*(9). doi: 10.1089/ast.2016.1629

Beuthe, M. (2018). Enceladus's crust as a non-uniform thin shell: I tidal deformations. *Icarus*, *302*. doi: 10.1016/j.icarus.2017.11.009

Cameron, M. E., Smith-Konter, B. R., Collins, G. C., Patthoff, D. A., & Pappalardo, R. T. (2019). Tidal stress modeling of Ganymede: Strike-slip tectonism and Coulomb failure. *Icarus*, *319*. doi: 10.1016/j.icarus.2018.09.002

CoreForm. (2020). "CUBIT" https://coreform.com/products/coreform-cubit/ .

Dahlen, F. A., & Tromp, J. (1998). *Theoretical global seismology.* doi: 10.1063/1.882788

Dai, C., Shum, C. K., Guo, J., Shang, K., Tapley, B., & Wang, R. (2016). Improved source parameter constraints for five undersea earthquakes from north component of GRACE gravity and gravity gradient change measurements. *Earth and Planetary Science Letters*, *443*. doi: 10.1016/j.epsl.2016.03.025

Ermakov, A. I., Park, R. S., Roa, J., Castillo-Rogez, J. C., Keane, J. T., Nimmo, F., ... Lainey, V. (2021). A recipe for the geophysical exploration of enceladus. *Planetary Science Journal*, *2*. doi: 10.3847/PSJ/ac06d2

Goldreich, P. M., & Mitchell, J. L. (2010). Elastic ice shells of synchronous moons: Implications for cracks on europa and non-synchronous rotation of titan. *Icarus*, *209*. doi: 10.1016/j.icarus.2010.04.013

Hansen, C. J., Esposito, L., Stewart, A. I., Colwell, J., Hendrix, A., Pryor, W., & Wast, R. (2006). Enceladus' water vapor plume. *Science*, *311*. doi: 10.1126/science.1121254

Hay, H. C., & Matsuyama, I. (2019). Nonlinear tidal dissipation in the subsurface oceans of enceladus and other icy satellites. *Icarus*, *319*. doi: 10.1016/j.icarus.2018.09.019

Hemingway, D. J., & Matsuyama, I. (2017). Isostatic equilibrium in spherical coordinates and implications for crustal thickness on the Moon, Mars, Enceladus, and elsewhere. *Geophysical Research Letters*, *44*(15). doi: 10.1002/2017GL073334

Hemingway, D. J., & Mittal, T. (2019). Enceladus's ice shell structure as a window on internal heat production. *Icarus*, *332*. doi: 10.1016/j.icarus.2019.03.011

Hoppa, G., Greenberg, R., Tufts, B. R., Geissler, P., Phillips, C., & Milazzo, M. (2000). Distribution of strike-slip faults on Europa. *Journal of Geophysical Research E: Planets*, *105*(E9). doi: 10.1029/1999JE001156

Hubbard, W. B., & Anderson, J. D. (1978). Possible flyby measurements of galilean satellite interior structure. *Icarus*, *33*. doi: 10.1016/0019-1035(78)90153-7

Hurford, T. A., Helfenstein, P., Hoppa, G. V., Greenberg, R., & Bills, B. G. (2007). Eruptions arising from tidally controlled periodic openings of rifts on enceladus. *Nature*, *447*. doi: 10.1038/nature05821

Iess, L., Stevenson, D. J., Parisi, M., Hemingway, D., Jacobson, R. A., Lunine, J. I., & Tortora, P. (2014). The gravity field and interior structure of Enceladus. *Science*, *344*(6179). doi: 10.1126/science.1250551

Ingersoll, A. P., Ewald, S. P., & Trumbo, S. K. (2020). Time variability of the enceladus plumes: Orbital periods, decadal periods, and aperiodic change. *Icarus*, *344*. doi: 10.1016/j.icarus.2019.06.006

Jaccard, C. (1976). P. v. hobbs ice physics. oxford, clarendon press, 1974. xvii, 837 p. £29. *Journal of Glaciology*, *17*. doi: 10.3189/s0022143000030847

Kalyanaraman, B., Meylan, M. H., Bennetts, L. G., & Lamichhane, B. P. (2020). A coupled fluid-elasticity model for the wave forcing of an ice-shelf. *Journal of Fluids and Structures*, *97*. doi: 10.1016/j.jfluidstructs.2020.103074

Levinson, M. (1981). A new rectangular beam theory. *Journal of Sound and Vibration*, *74*. doi: 10.1016/0022-460X(81)90493-4

Love, A. E. H. (1909). The yielding of the earth to disturbing forces. *Proceedings of the Royal Society of London. Series A, Containing Papers of a Mathematical and Physical Character*, *82*. doi: 10.1098/rspa.1909.0008

McKinnon, W. B. (2015). Effect of enceladus's rapid synchronous spin on interpretation of cassini gravity. *Geophysical Research Letters*, *42*. doi: 10.1002/2015GL063384

McKinnon, W. B., & Melosh, H. J. (1980). Evolution of planetary lithospheres: Evidence from multiringed structures on Ganymede and Callisto. *Icarus*, *44*(2). doi: 10.1016/0019-1035(80)90037-8

Melosh, H. J., & Raefsky, A. (1981). A simple and efficient method for introducing faults into finite element computations. *Bulletin of the Seismological Society of America*, *71*(5). doi: 10.1785/bssa0710051391

Mitri, G., & Showman, A. P. (2005, 10). Convective–conductive transitions and sensitivity of a convecting ice shell to perturbations in heat flux and tidal-heating rate: Implications for Europa. *Icarus*, *177*(2), 447–460. doi: 10.1016/J.ICARUS.2005.03.019

Murray, C. D., & Dermott, S. F. (2000). *Solar System Dynamics*. doi: 10.1017/cbo9781139174817

Neumeier, J. J. (2018). Elastic constants, bulk modulus, and compressibility of h2o ice i h for the temperature range 50 k-273 k. *Journal of Physical and Chemical Reference Data*, *47*. doi: 10.1063/1.5030640

Nimmo, F., Bills, B. G., & Thomas, P. C. (2011). Geophysical implications of the long-wavelength topography of the Saturnian satellites. *Journal of Geophysical Research E: Planets*, *116*(11). doi: 10.1029/2011JE003835

Nimmo, F., Thomas, P. C., Pappalardo, R. T., & Moore, W. B. (2007). The global shape of europa: Constraints on lateral shell thickness variations. *Icarus*, *191*. doi: 10.1016/j.icarus.2007.04.021

Porco, Dinino, D., & Nimmo, F. (2014). How the geysers, tidal stresses, and thermal emission across the south polar terrain of enceladus are related. *Astronomical Journal*, *148*. doi: 10.1088/0004-6256/148/3/45

Porco, Helfenstein, P., Thomas, P. C., Ingersoll, A. P., Wisdom, J., West, R., & Squyres, S. (2006). Cassini observes the active south pole of enceladus. *Science*, *311*. doi: 10.1126/science.1123013

Ramillien, G., Cazenave, A., & Brunau, O. (2004). Global time variations of hydrological signals from grace satellite gravimetry. *Geophysical Journal International*, *158*. doi: 10.1111/j.1365-246X.2004.02328.x

Roberts, J. H., & Nimmo, F. (2008, 4). Tidal heating and the long-term stability of a subsurface ocean on Enceladus. *Icarus*, *194*(2), 675–689. doi: 10.1016/J.ICARUS.2007.11.010

Schenk, P. M. (2008). Cartographic and Topographic Mapping of the Icy Satellites of the Outer Solar System. *International Archives of the Photogrammetry, Remote Sensing and Spatial Information Sciences*, *37*.

Schenk, P. M., Clark, R. N., Howett, C. J. A., Verbiscer, A. J., & Waite, J. H. (2018). *Enceladus and the icy moons of saturn.* doi: 10.2458/azu_uapress_9780816537075

Schubert, G., Anderson, J. D., Travis, B. J., & Palguta, J. (2007). Enceladus: Present internal structure and differentiation by early and long-term radiogenic heating. *Icarus*, *188*(2). doi: 10.1016/j.icarus.2006.12.012

Segall, P. (2010). *Earthquake and volcano deformation.* doi: 10.5860/choice.48-0287

Shaw, G. H. (1985). Elastic properties and equation of state of high pressure ice. *The Journal of Chemical Physics*, *84*. doi: 10.1063/1.449897

Simons, M., & Rosen, P. A. (2015). Interferometric Synthetic Aperture Radar Geodesy. In *Treatise on geophysics: Second edition* (Vol. 3). doi: 10.1016/B978-0-444-53802-4.00061-0

Skroch, M., Owen, S., Staten, M., Quadros, R., Hanks, B., Clark, B., & Stimpson, C. (2019). *CUBIT Geometry and Mesh Generation Toolkit 15.4 User Documentation.*

Souček, O., Běhounková, M., Čadek, O., Hron, J., Tobie, G., & Choblet, G. (2019). Tidal dissipation in Enceladus' uneven, fractured ice shell. *Icarus*, *328*. doi: 10.1016/j.icarus.2019.02.012

Souček, O., Hron, J., Běhounková, M., & Čadek, O. (2016). Effect of the tiger stripes on the deformation of Saturn's moon Enceladus. *Geophysical Research Letters*, *43*(14). doi: 10.1002/2016GL069415

Spencer, J. R., Pearl, J. C., Segura, M., Flasar, F. M., Mamoutkine, A., Romani, P., & Lopes, R. M. (2006). Cassini encounters enceladus: Background and the discovery of a south polar hot spot. *Science*, *311*. doi: 10.1126/science.1121661

Thomas, P. C., Tajeddine, R., Tiscareno, M. S., Burns, J. A., Joseph, J., Loredo, T. J., & Porco, C. (2016). Enceladus's measured physical libration requires a global subsurface ocean. *Icarus*, *264*. doi: 10.1016/j.icarus.2015.08.037

Tyler, R. H. (2020). Heating of enceladus due to the dissipation of ocean tides. *Icarus*, *348*. doi: 10.1016/j.icarus.2020.113821

Vance, S., Behounkova, M., Bills, B. G., Byrne, P., Cadek, O., Castillo-Rogez, J., ... Wang, S. (2021). Distributed geophysical exploration of enceladus and other ocean worlds. *Bulletin of the AAS*, *53*. doi: 10.3847/25c2cfeb.a07234f4

Wahr, Selvans, Z. A., Mullen, M. E., Barr, A. C., Collins, G. C., Selvans, M. M., & Pappalardo, R. T. (2009). Modeling stresses on satellites due to nonsynchronous rotation and orbital eccentricity using gravitational potential theory. *Icarus*, *200*(1). doi: 10.1016/j.icarus.2008.11.002

Wahr, Zuber, M. T., Smith, D. E., & Lunine, J. I. (2006). Tides on Europa, and the thickness of Europa's icy shell. *Journal of Geophysical Research E: Planets*, *111*(12). doi: 10.1029/2006JE002729

Yin, A., & Pappalardo, R. T. (2015). Gravitational spreading, bookshelf faulting, and tectonic evolution of the South Polar Terrain of Saturn's moon Enceladus. *Icarus*, *260*. doi: 10.1016/j.icarus.2015.07.017

Zolotov, M. Y., & Shock, E. L. (2004). A model for low-temperature biogeochemistry of sulfur, carbon, and iron on Europa. *Journal of Geophysical Research E: Planets*, *109*(6). doi: 10.1029/2003JE002194

Čadek, O., Tobie, G., Van Hoolst, T., Lefèvre, A., Mitri, G., Běhounková, M., & Trinh, A. (2016). Enceladus's internal ocean and ice shell constrained from cassini gravity, shape, and libration data. *Geophysical Research Letters*, *43*. doi: 10.1002/2016GL068634

Figure 1.

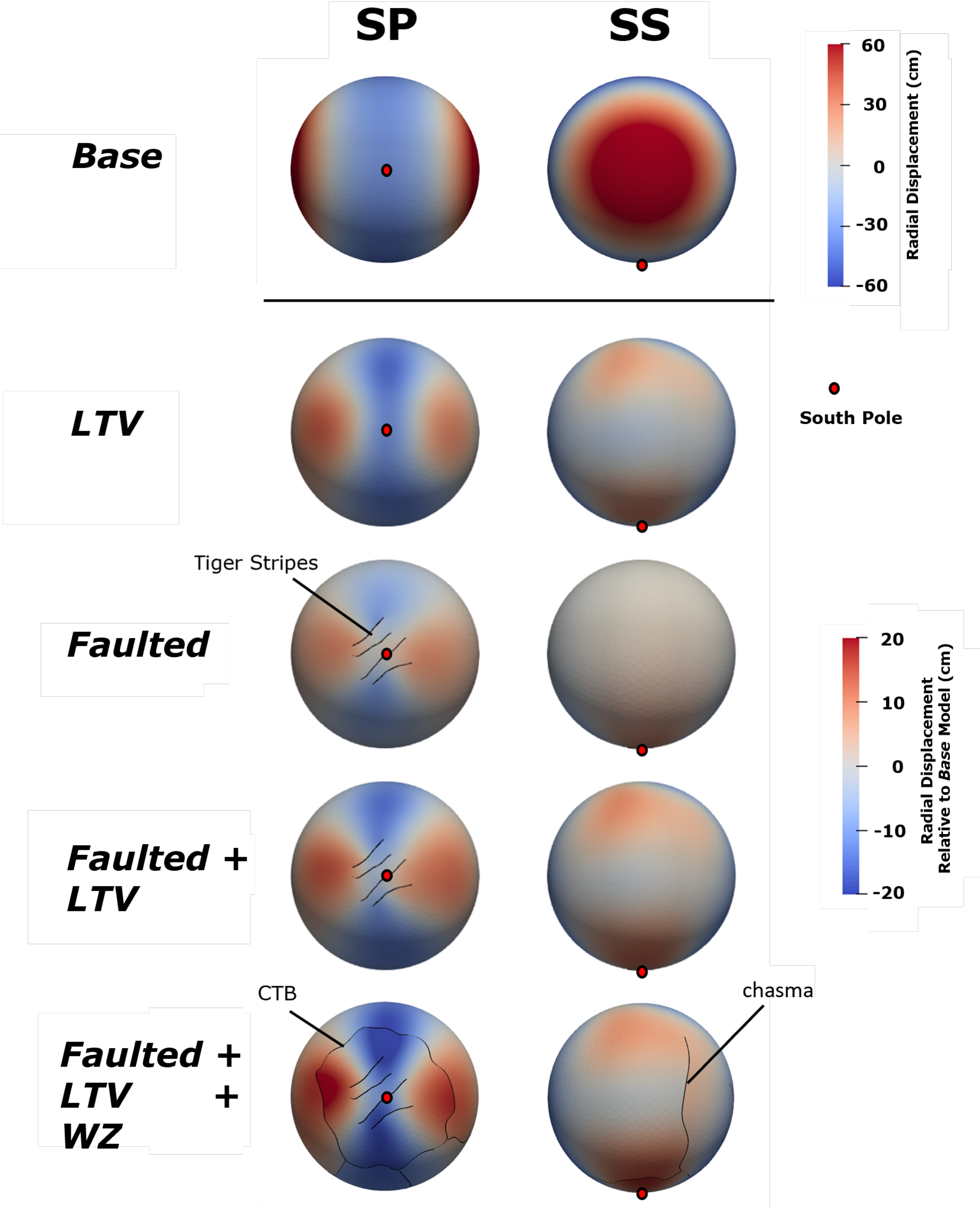

SP
SS
Base
LTV
Faulted
Faulted + LTV
Faulted + LTV + WZ
Tiger Stripes
CTB
chasma
60
30
0
-30
-60
Radial Displacement (cm)
South Pole
20
10
0
-10
-20
Radial Displacement Relative to Base Model (cm)

Figure 3.

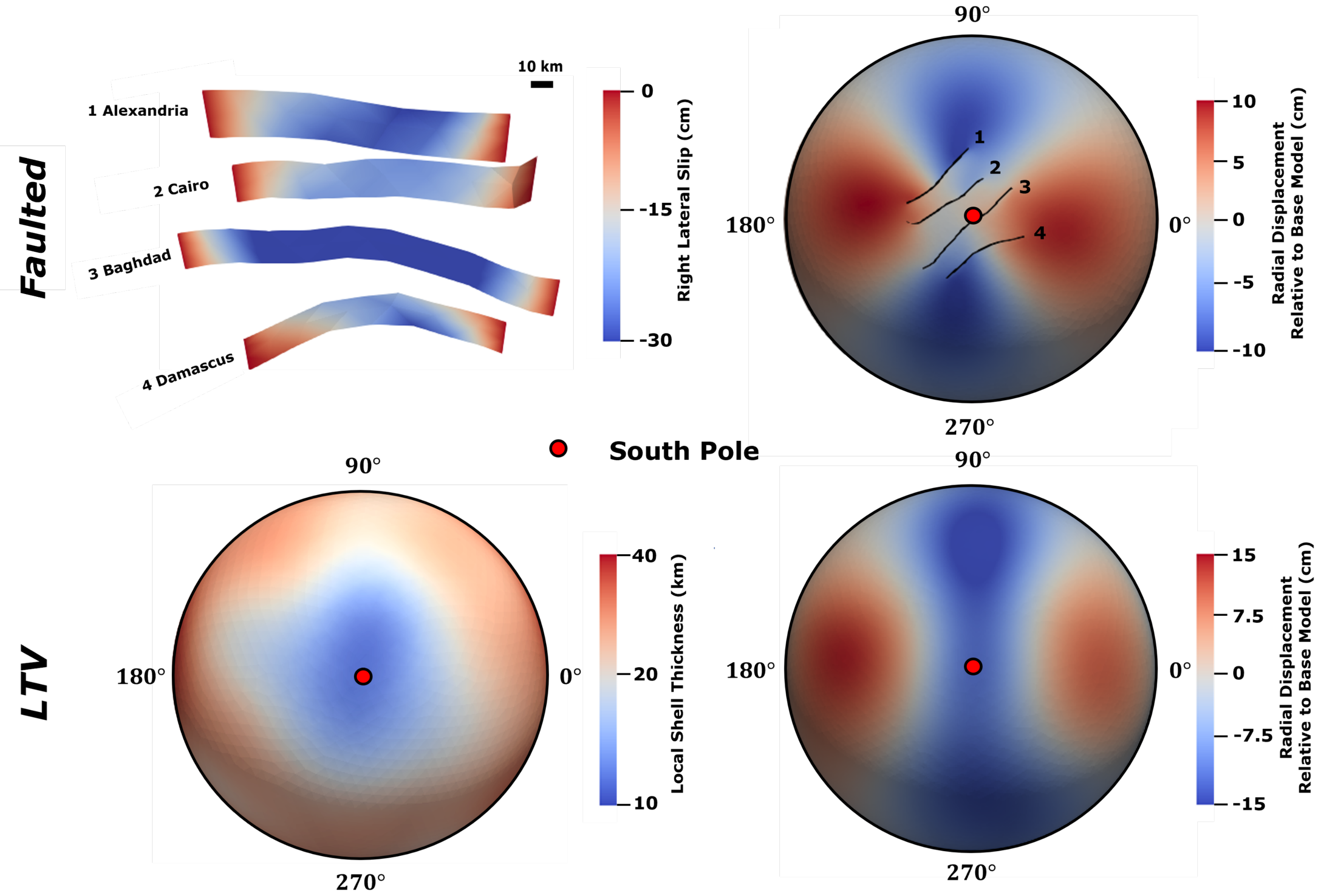

Faulted
LTV
1 Alexandria
2 Cairo
3 Baghdad
4 Damascus
10 km
0
-15
-30
Right Lateral Slip (cm)
90°
180°
0°
270°
1
2
3
4
10
5
0
-5
-10
Radial Displacement Relative to Base Model (cm)
South Pole
40
20
10
Local Shell Thickness (km)
15
7.5
0
-7.5
-15

Figure 4.

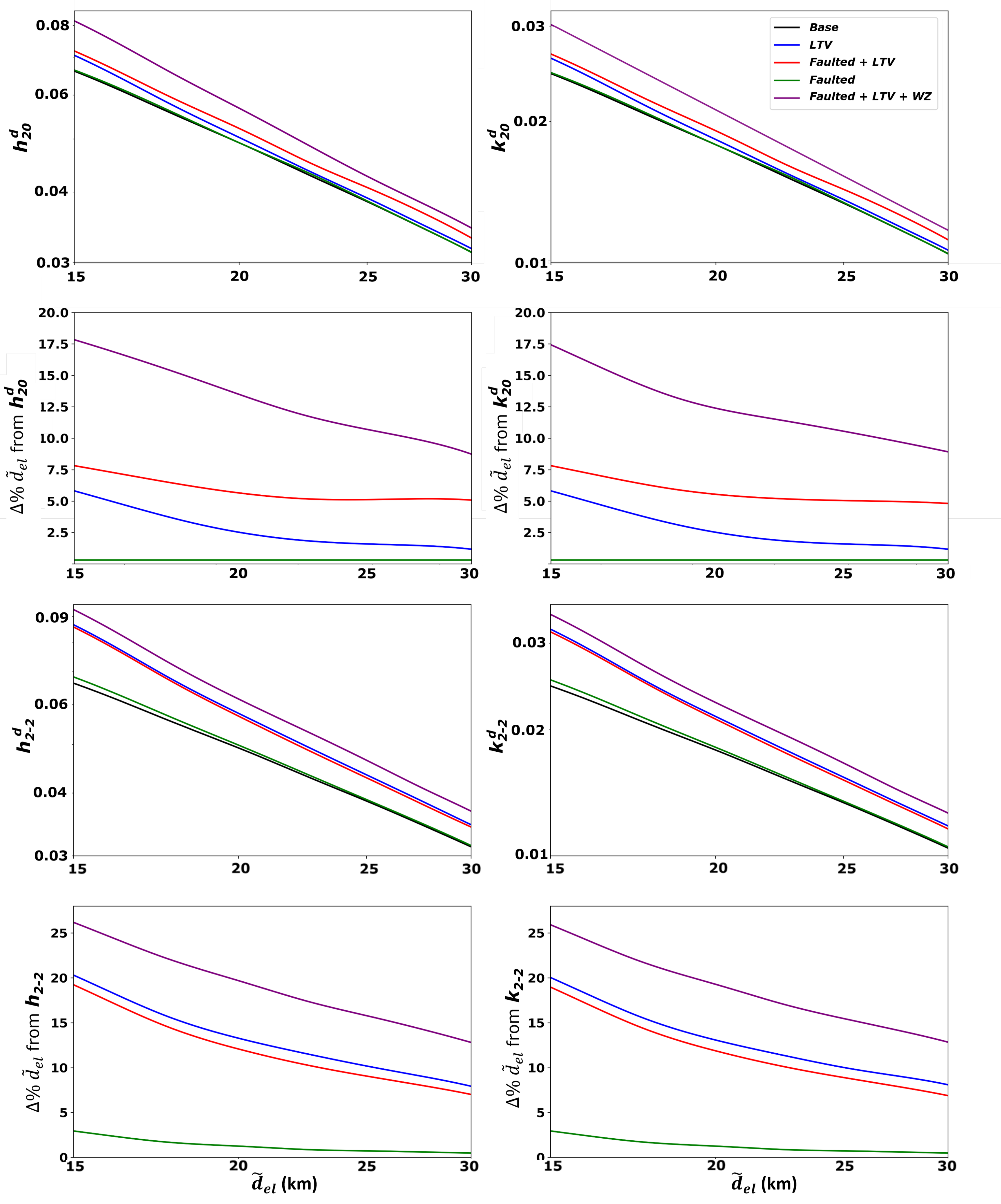

Base
LTV
Faulted + LTV
Faulted
Faulted + LTV + WZ
h^d_{20}
k^d_{20}
$\Delta\%\ \tilde{d}_{el}$ from h^d_{20}
$\Delta\%\ \tilde{d}_{el}$ from k^d_{20}
$h^d_{2\text{-}2}$
$k^d_{2\text{-}2}$
$\Delta\%\ \tilde{d}_{el}$ from $h_{2\text{-}2}$
$\Delta\%\ \tilde{d}_{el}$ from $k_{2\text{-}2}$
$\tilde{d}_{el}$ (km)

Figure 2.

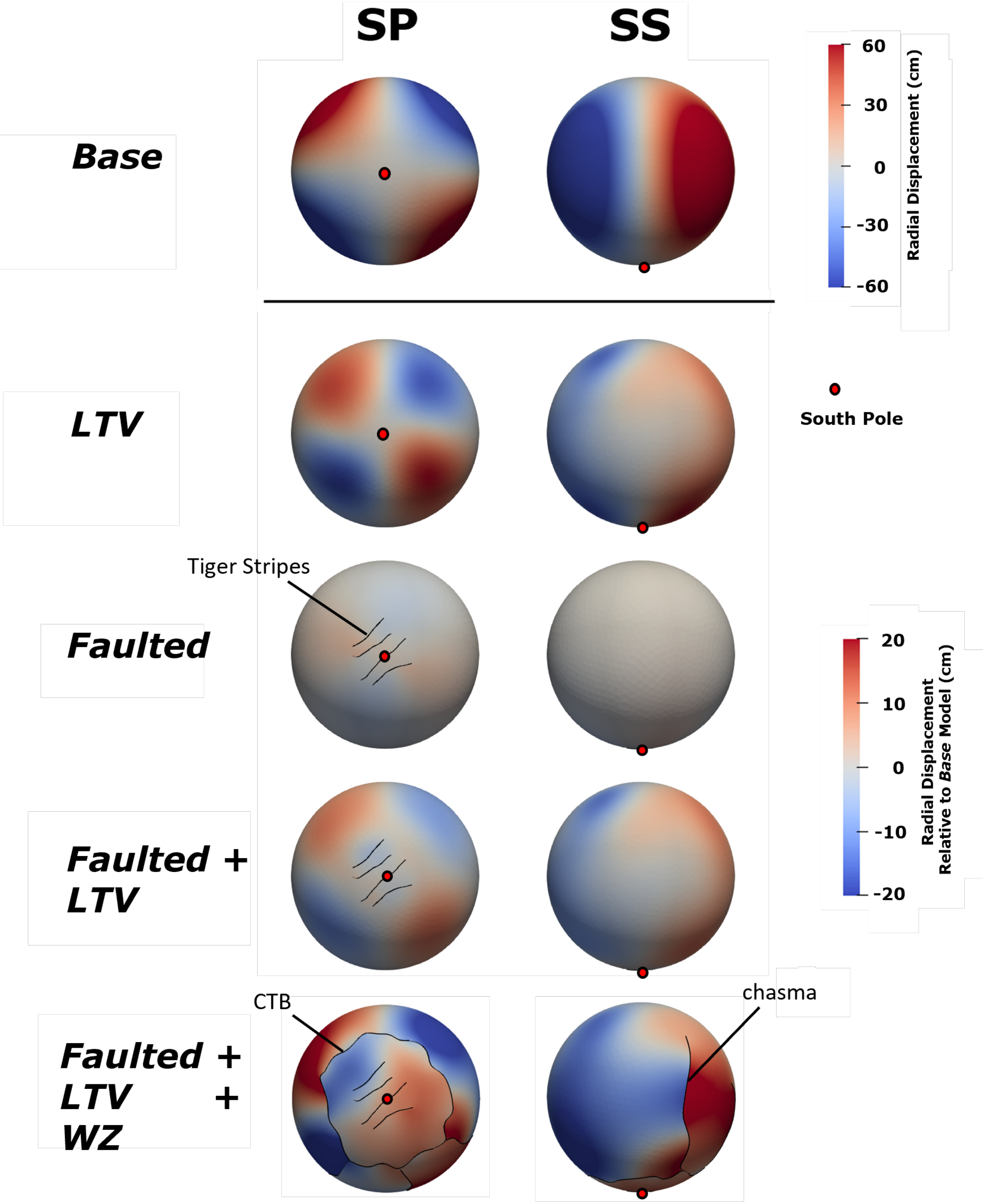
SP
SS
Base
LTV
Faulted
Faulted + LTV
Faulted + LTV + WZ
Tiger Stripes
CTB
chasma
South Pole
Radial Displacement (cm)
60
30
0
-30
-60
Radial Displacement Relative to Base Model (cm)
20
10
0
-10
-20

Figure 5.

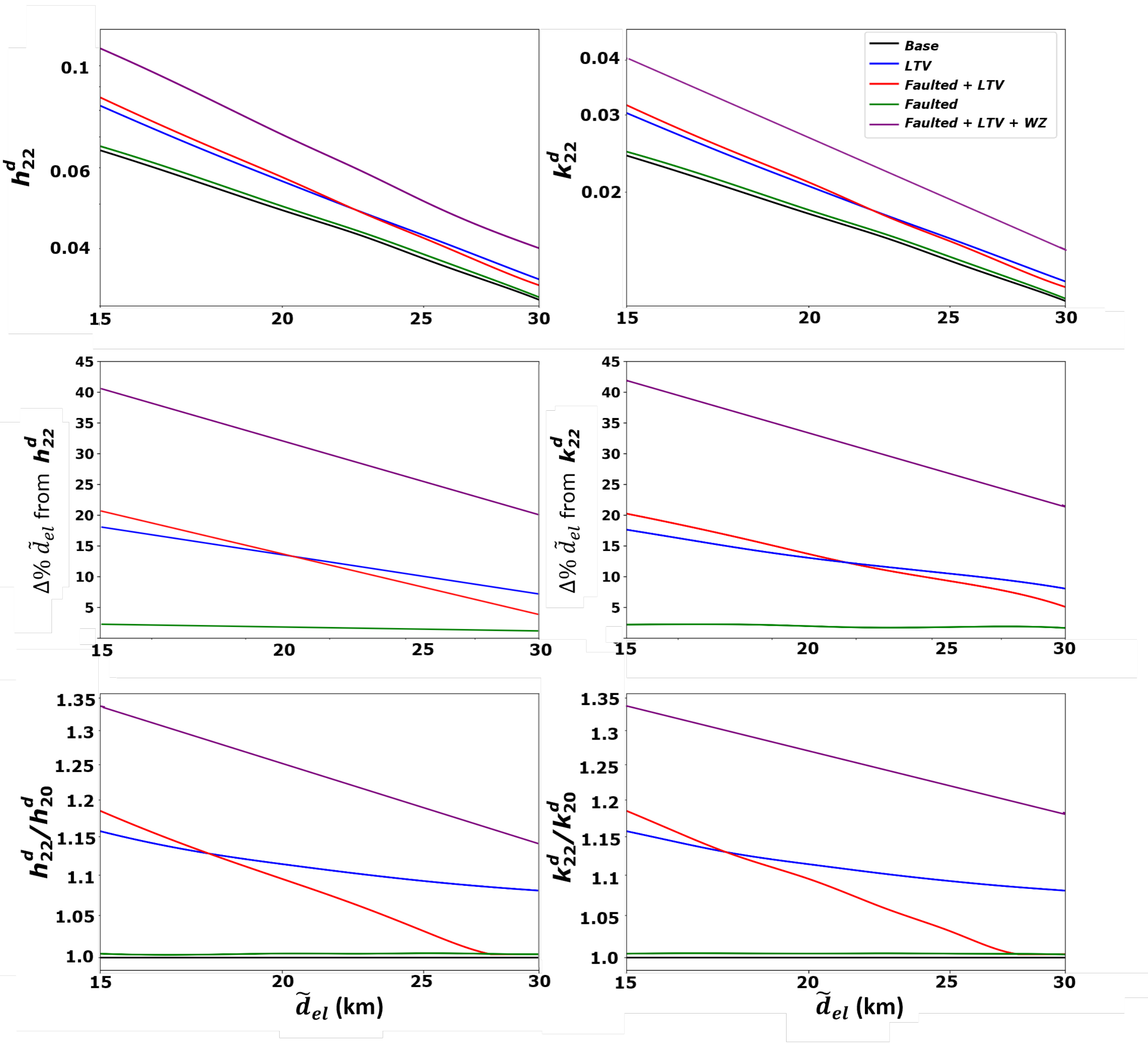
Base
LTV
Faulted + LTV
Faulted
Faulted + LTV + WZ
h^d_{22}
k^d_{22}
$\Delta\%\ \tilde{d}_{el}$ from h^d_{22}
$\Delta\%\ \tilde{d}_{el}$ from k^d_{22}
h^d_{22}/h^d_{20}
k^d_{22}/k^d_{20}
$\tilde{d}_{el}$ (km)

Supplementary Documentation for "Inferring the Mean Effective Elastic Thickness of the Outer Ice Shell of Enceladus from Diurnal Crustal Deformation"

In S1, we describe the governing equations for our tidal loading boundary value problem and our solution method (1.1), benchmark our solutions against analytic and numerical tidal loading models (1.2), and verify that results on models with heterogeneities are not subject to inaccuracy due to our choice of mesh sizing parameters (1.3) or our choice of weak-zone elastic moduli (1.4).

S1

1.1 Tidal Loading Formulation

Following Aagaard et al. (2007), we formulate and solve a boundary value problem appropriate for tidal loading. We solve the weak form the quasi-static equation of motion in cartesian directions i for a body subject to stresses σ_{ij} and specific forces f_i over the volume W and a weighting function ϕ_i (the symbol , denotes derivative with respect to a direction):

$$\int_W (\sigma_{ij,j} + f_i)\ \phi_i\ dW = 0 \tag{1}$$

Following the Galerkin approach, we formulate our weighting function ϕ_i as an n-dimensional linear combination of linear basis (i.e., shape) functions N^n scaled by coefficients c_i^n and our trial solution (i.e., for displacement u_i) as an m-dimensional linear combination of linear basis functions N^m scaled by coefficients a_i^m :

$$\phi_i = \sum_n c_i^n N^n \tag{2a}$$

$$u_i = \sum_m a_i^m N^m \tag{2b}$$

Considering the divergence theorem for stresses in W, substituting our formulation for the weighting function, and recognizing that the equation of motion's weak form is equivalent to the strong form for arbitrary weighting function coefficients c_i^n allows us to rewrite Equation 1 as a sum of integrals over surfaces S subject to tractions T_i and over W subject to specific forces f_i:

$$-\int_W \sigma_{ij} N^n_{,j} dW \ + \int_S T_i N^n dS \ + \int_W f_i N^n dW = 0 \tag{3}$$

We expand each term in Equation 3 according to our tidal loading formulation. We rewrite the first term (from the left) as a combination of shape functions scaled by a rank-4 stiffness tensor C_{ijqw}. We select parameters in C_{ijqw} appropriate for a linear isotropic material with a shear modulus G and bulk modulus μ:

$$-\int_W \sigma_{ij} N^n_{,j} dW = \int_W \sum_m \frac{1}{4} C_{ijqw} (N^m_{,w} + N^m_{,q})(N^n_{,j} + N^n_{,i}) a^m_i dW \tag{4}$$

We subdivide the second term of Equation 3 to treat tractions at the outer surface S^0 (i.e., T^0_i) and the inner surface S^{int} (i.e., T^{int}_i) of our geometry. For small displacements induced by a loading potential V (See Equation 2 of the main text), we can write T^{int}_i and T^0_i as dependent upon radial displacements at the boundaries of our geometry $\sum_m a^m_i N^m(\mathbf{e}_i \cdot \mathbf{e}_s)$ (see Equation 2; $\mathbf{e}_i$ and $\mathbf{e}_s$ respectively denote unit vectors perpendicular to the surface of the geometry and the evaluated direction), the density of ice ρ_{ice} and ocean water ρ_w, gravitational acceleration at the inner and outer surfaces g_{int} and g_0 (see Table 2 in the main text), and self-gravitation induced by radial displacements throughout our geometry V^{sg}. Here, we treat self-gravitational potential V^{sg} as resulting from small perturbations to the driving potential V and therefore as a separate (i.e., uncoupled) term as per Taylor's approximation theorem:

$$\int_{S^0} T^0_i N^n dS = \int_{S^0} \sum_m a^m_i N^m (\mathbf{e}_i \cdot \mathbf{e}_s) \rho_{ice} g_0 (\mathbf{e}_s \cdot \mathbf{e}_i) N^n dS \tag{5a}$$

$$\int_{S^{int}} T^{int}_i N^n dS = \int_{S^{int}} (\sum_m a^m_i N^m (\mathbf{e}_i \cdot \mathbf{e}_s)(\rho_{ice} - \rho_w) g_{int} + \rho_w V + \rho_w V^{sg})(\mathbf{e}_s \cdot \mathbf{e}_i) N^n dS \tag{5b}$$

The specific force (i.e., third) term in Equation 3 is rewritten as the gradient of the driving and self-gravitational potentials scaled by ice density as per Newton's second law:

$$\int_W f_i N^n dW = \int_W (\rho_{ice} \nabla (V + V^{sg}) \cdot \mathbf{e}_i) N^n dW \tag{6}$$

Terms from Equations 6, 5a, and 5b constitute the 'body' F^b, 'ocean traction' F^o, and 'topographic' F^t forces discussed in Section 2.2 of the main text (see supplementary equation S5 of Souček et al. 2016):

$$F^b = \int_W (\rho_{ice} \nabla (V + V^{sg}) \cdot \mathbf{e}_i) N^n dW \tag{7a}$$

$$F^o = \int_{S^{int}} (\rho_w V + \rho_w V^{sg})(\mathbf{e}_s \cdot \mathbf{e}_i) N^n dS \tag{7b}$$

$$\begin{aligned} F^t = &\int_{S^0} \sum_m a_i^m N^m (\mathbf{e}_i \cdot \mathbf{e}_s) \rho_{ice} g_0 (\mathbf{e}_s \cdot \mathbf{e}_i) N^n dS \\ + &\int_{S^{int}} (\sum_m a_i^m N^m (\mathbf{e}_i \cdot \mathbf{e}_s)(\rho_{ice} - \rho_w) g_{int})(\mathbf{e}_s \cdot \mathbf{e}_i) N^n dS \end{aligned} \tag{7c}$$

To compute V^{sg}, we combine solutions to the Poisson's equation (i.e., potentials) evaluated at nodes with radial locations r^n arising from displacements linearly mapped into spherical harmonics at inner V_0^{sg} and outer surfaces V_{int}^{sg} (i.e., via the rank-4 tensors H^0_{lknm} and H^{int}_{lknm} evaluated at mean radial locations R_{int} and R_0 respectively with degree l and order k) and universal gravitational constant $\mathcal{G}$ (i.e., as discussed in Hemingway & Mittal (2019) cf. Equation 4). We assume V^{sg} arises purely from the movement of mass at the boundaries of our domain (i.e., the inner and outer surfaces of the crust) and so ignore effects due to the changes in density on V^{sg}:

$$V^{sg} = V_{int}^{sg} + V_0^{sg} \tag{8}$$

$$V_{int}^{sg} = \sum_l \sum_k \frac{4\pi \mathcal{G} r^n}{2l+1} (\rho_w - \rho_{ice}) \sum_m H^0_{lknm} a_i^m N^m (\mathbf{e}_i \cdot \mathbf{e}_s) (\frac{R_0}{r^n})^{l+2} \tag{9a}$$

$$V_0^{sg} = \sum_l \sum_k \frac{4\pi \mathcal{G} r^n}{2l+1} \rho_{ice} \sum_m H^{int}_{lknm} a_i^m N^m (\mathbf{e}_i \cdot \mathbf{e}_s) (\frac{r^n}{R_{int}})^{l-1} \tag{9b}$$

We combine terms from Equations 4, 5a, 5b, 6, 8, and 9 to formulate a Jacobian A_{ij}^{nm} as a superposition of tensors integrated over our domain volume ${}_W A_{ij}^{nm}$, outer surface ${}_{S^0} A_{ij}^{nm}$, and inner surface ${}_{S^{int}} A_{ij}^{nm}$.

$$A_{ij}^{nm} = {}_W A_{ij}^{nm} + {}_{S^0} A_{ij}^{nm} + {}_{S^{int}} A_{ij}^{nm} \tag{10}$$

$$
{}_{W}A_{ij}^{nm} = \int_{V} (\frac{1}{4}C_{ijqw}(N_{,w}^{m} + N_{,q}^{m})(N_{,j}^{n} + N_{,i}^{n}) + (\rho_{ice}\nabla(\sum_{l}\sum_{k}\frac{4\pi\mathcal{G}r^{n}}{2l+1}((\rho_{w} - \rho_{ice})
H_{lknm}^{0}(\mathbf{e}_{i}\cdot\mathbf{e}_{s})(\frac{R_{0}}{r^{n}})^{l+2} + \rho_{ice}H_{lknm}^{int}(\mathbf{e}_{i}\cdot\mathbf{e}_{s})(\frac{r^{n}}{R_{int}})^{l-1}))\cdot\mathbf{e}_{i})N^{n}N^{m})dW \tag{11a}
$$

$$
{}_{S^{int}}A_{ij}^{nm} = \int_{S^{int}} ((\rho_{w}\sum_{l}\sum_{k}\frac{4\pi\mathcal{G}r^{n}}{2l+1}((\rho_{w} - \rho_{ice})H_{lknm}^{0}(\mathbf{e}_{i}\cdot\mathbf{e}_{s})(\frac{R_{0}}{r^{n}})^{l+2} + \rho_{ice}H_{lknm}^{int}
(\mathbf{e}_{i}\cdot\mathbf{e}_{s})(\frac{r^{n}}{R_{int}})^{l-1}))(\mathbf{e}_{s}\cdot\mathbf{e}_{i}) + (\mathbf{e}_{i}\cdot\mathbf{e}_{s})(\rho_{ice} - \rho_{w})g_{int}(\mathbf{e}_{s}\cdot\mathbf{e}_{i}))N^{n}N^{m}dS \tag{11b}
$$

$$
{}_{S^{0}}A_{ij}^{nm} = \int_{S^{0}} (\mathbf{e}_{i}\cdot\mathbf{e}_{s})\rho_{ice}g_{0}(\mathbf{e}_{s}\cdot\mathbf{e}_{i})N^{n}N^{m}dS \tag{11c}
$$

We can also combine terms from Equations 5a, 5b, and 6 to write a force vector b_i^n:

$$
b_{i}^{n} = -\int_{W}(\rho_{ice}\nabla V\cdot\mathbf{e}_{i})N^{n}dW - \int_{S^{int}}\rho_{w}V(\mathbf{e}_{s}\cdot\mathbf{e}_{i})N^{n}dS \tag{12}
$$

Finally, we assemble Equations 10, 11, and 12 to form a linear system and solve for displacement coefficients a_i^m.

$$
A_{ij}^{nm}a_{i}^{m} = b_{i}^{n} \tag{13}
$$

1.2 Benchmarking

We benchmark our tidal loading formulation on *Base* models against analytic solutions using the spectral solver software package SATStress, a widely used tool within the planetary science community to predict diurnal (and fluid) Love number values and stress fields on planetary bodies (Wahr et al., 2009). SATStress solves the equation of motion for tidally-loaded multi-layered spherically symmetric bodies accounting for self-gravitation and viscous effects. Figure 1 shows predictions of Love number values from SATStress across our range of modelled $\tilde{d}_{el}$ values. Within SATStress, we specify a multi-layered body with an outer ice layer and underlying ocean consistent with the rheological parameters in Table 2 (see main text), an ice viscosity ν = 1e16 Pa-s (Friedson & Stevenson, 1983), an ocean shear modulus G_o = 1e-20 GPa, and an ocean viscosity ν_o = 1e-20 Pa-s. Love number values between numerical and analytical models agree to within <0.1% across all $\tilde{d}_{el}$ values. Possible additional minor differences between predictions

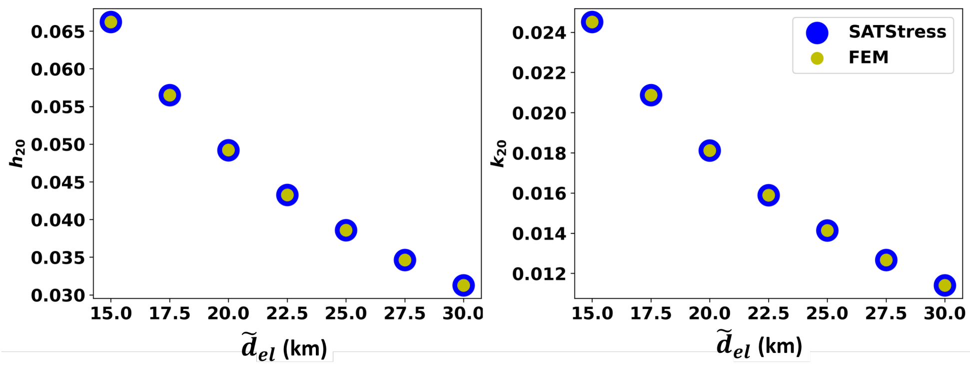

Figure 1. Comparison of analytic and FEM Love number results for several values of $\tilde{d}_{el}$ on spherically symmetric (*Base*) models. Love numbers plotted against $\tilde{d}_{el}$ for analytic models using SATStress (blue dots) and using the FEM formulated here (yellow dots).

from either set of results may result from our lack of accounting for changes in ice shell rheology due to volumetric expansion/contraction or viscous effects within the ice shell during tidal loading (See Wahr et al. (2006), for details).

We additionally compare model results from this work with results from Souček et al. (2016). Figure 2 shows displacement magnitude fields at three different time indices in the tidal cycle (t=0.0 T (periapse) , 0.2 T, and 0.4 T, where T is the orbital period T = 33 hrs) for models in Souček et al. (2016) (top row) and this work (bottom). We deactivate self-gravitation on *Base* models assign weak zones (with assigned bulk modulus $\mu_{WZ} = 10^{-5}\mu$ and shear modulus $G_{WZ} = 10^{-5}G$) to regions surrounding the Tiger Stripes for model comparisons. We find we are able to largely reproduce results from Souček et al., (2016) both quantitatively (i.e., peak displacement magnitude values correspond to within <10%) and qualitatively. Slight differences in displacement field characteristics persist surrounding the weak zone regions due to methodological differences in the implementation of adaptive mesh sizing, the assignment of reduced elastic moduli (i.e., the location of the Tiger Stripes and the shear modulus reduction away from fault planes), or the use of different shape functions (i.e., linear vs. quadratic) between models.

1.3 Mesh Convergence Test

We perform a mesh convergence test to confirm that Love number results from models with structural heterogeneities are not sensitive to chosen mesh sizing parameters. Figure 3 shows Love number values evaluated from models with only weak zones at chasma,

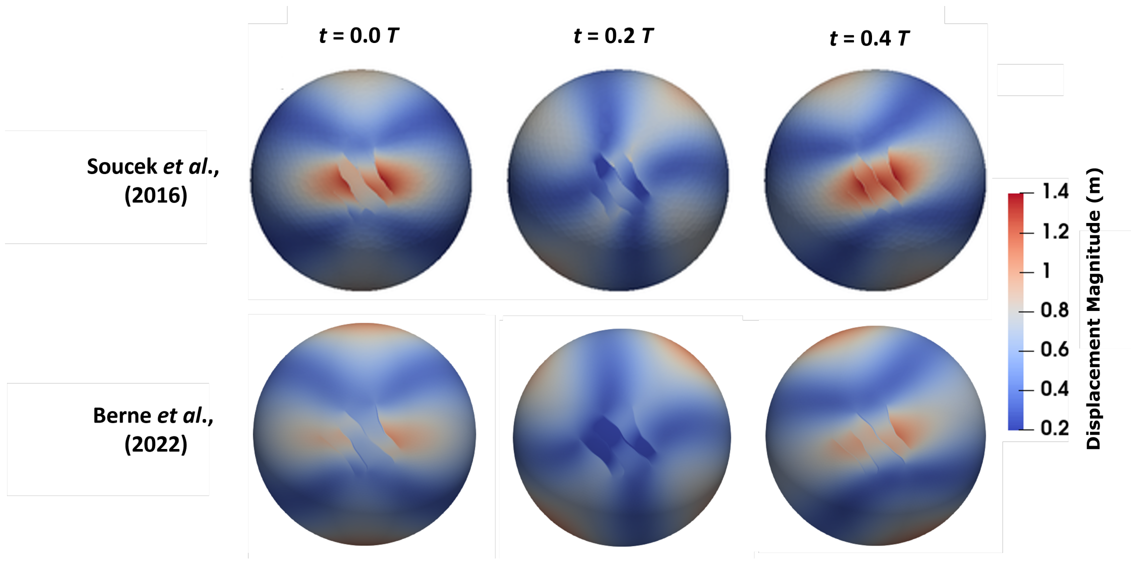

Figure 2. Qualitative comparison of our FEM results with results from Souček et al. (2016) (top row) and this work (bottom row) for models with weak zones at Tiger Stripe locations viewed facing the South Pole. Fields denote the magnitude of the displacement vector evaluated at the outer surface of deformed geometries. The top row and colorbar of this Figure adapted from top row of Figure 3 of Souček et al. (2016). We assign weak zone bulk moduli μ_{WZ}/μ=10^{-5} and shear moduli G_{WZ}/G=10^{-5} for our simulations in accordance with the formulation of weak zones described in Souček et al. (2016).

Tiger Stripe, and circum-tectonic boundary locations (i.e., *WZ* models) and $\tilde{d}_{el} = 15$ km meshed with specified minimum cell side lengths S_{min}= 6, 5, 4, 3, 2, and 1 km. We additionally show example snapshots of the radial displacement fields between our *WZ* model relative to our *Base* model for geometries with $\tilde{d}_{el} = 15$ km across our range of tested S_{min} values. Results from Figure 3 demonstrate that both Love number results and overall radial displacement fields are insensitive to chosen minimum cell size for values of $S_{min} <$ 3 km. We accordingly assign $S_{min} = 1$ km for all models discussed in this work.

1.4 Choice of Weak Zone Elastic Parameters

We evaluate results from models with weak zones at chasma, Tiger Stripe, and circum-tectonic boundary locations (i.e., *WZ* models) to confirm that Love number outputs are not sensitive to our choice of weak zone shear modulus. Figure 4 shows Love number values evaluated from *WZ* models with $\tilde{d}_{el} = 15$ km and specified weak zone moduli across $10^{-8} < G_{WZ}/G < 10^{0}$. We additionally show example snapshots of radial displacement fields from our *WZ* models relative to our *Base* model with $\tilde{d}_{el} = 15$ km across our range of tested G_{WZ} values. Results from Figure 4 demonstrate that both Love number results and overall radial displacement fields are insensitive weak zone shear modulus for $G_{WZ}/G < 10^{-4}$. These results are consistent with those described in the supplementary documentation of Souček et al. (2016) but extend to inferences of displacement away from the Tiger Stripes and for instances of non-zero bulk modulus within weak zones.

References

Aagaard, B., Williams, C., & Knepley, M. (2007). PyLith: A Finite-Element Code for Modeling Quasi-Static and Dynamic Crustal Deformation. *Eos*, *88(52)*.

Friedson, A. J., & Stevenson, D. J. (1983). Viscosity of rock-ice mixtures and applications to the evolution of icy satellites. *Icarus*, *56*. doi: 10.1016/0019-1035(83)90124-0

Hemingway, D. J., & Mittal, T. (2019). Enceladus's ice shell structure as a window on internal heat production. *Icarus*, *332*. doi: 10.1016/j.icarus.2019.03.011

Souček, O., Hron, J., Běhounková, M., & Čadek, O. (2016). Effect of the tiger stripes on the deformation of Saturn's moon Enceladus. *Geophysical Research*

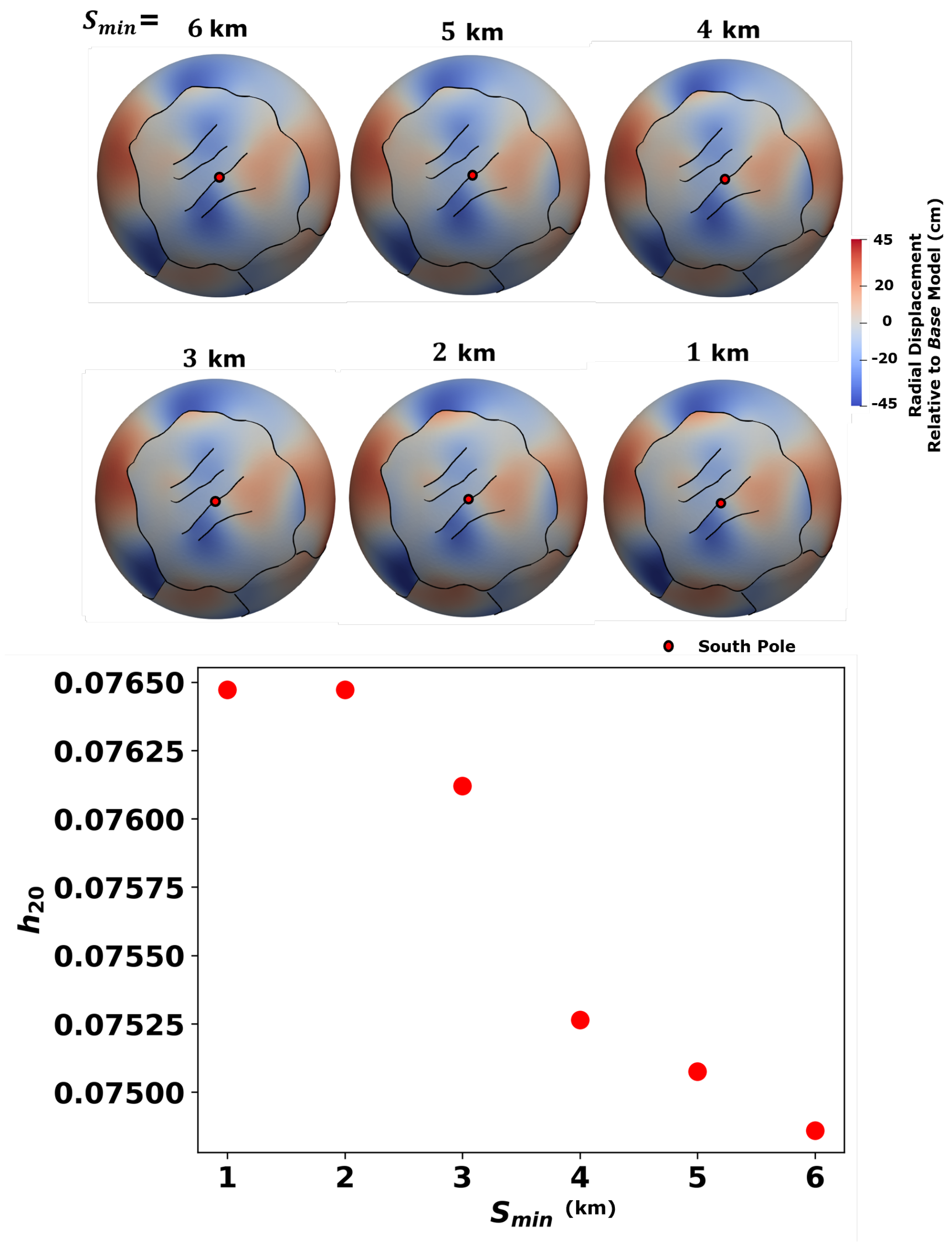

Figure 3. Results evaluated at periapse for *WZ* models ($\tilde{d}_{el}$ = 15 km) for a range of S_{min}. We show radial displacement fields viewed facing upwards towards the South Pole (top) and h^d_{20} Love number results we use to track the sensitivity of results due to changes in S_{min} (bottom)

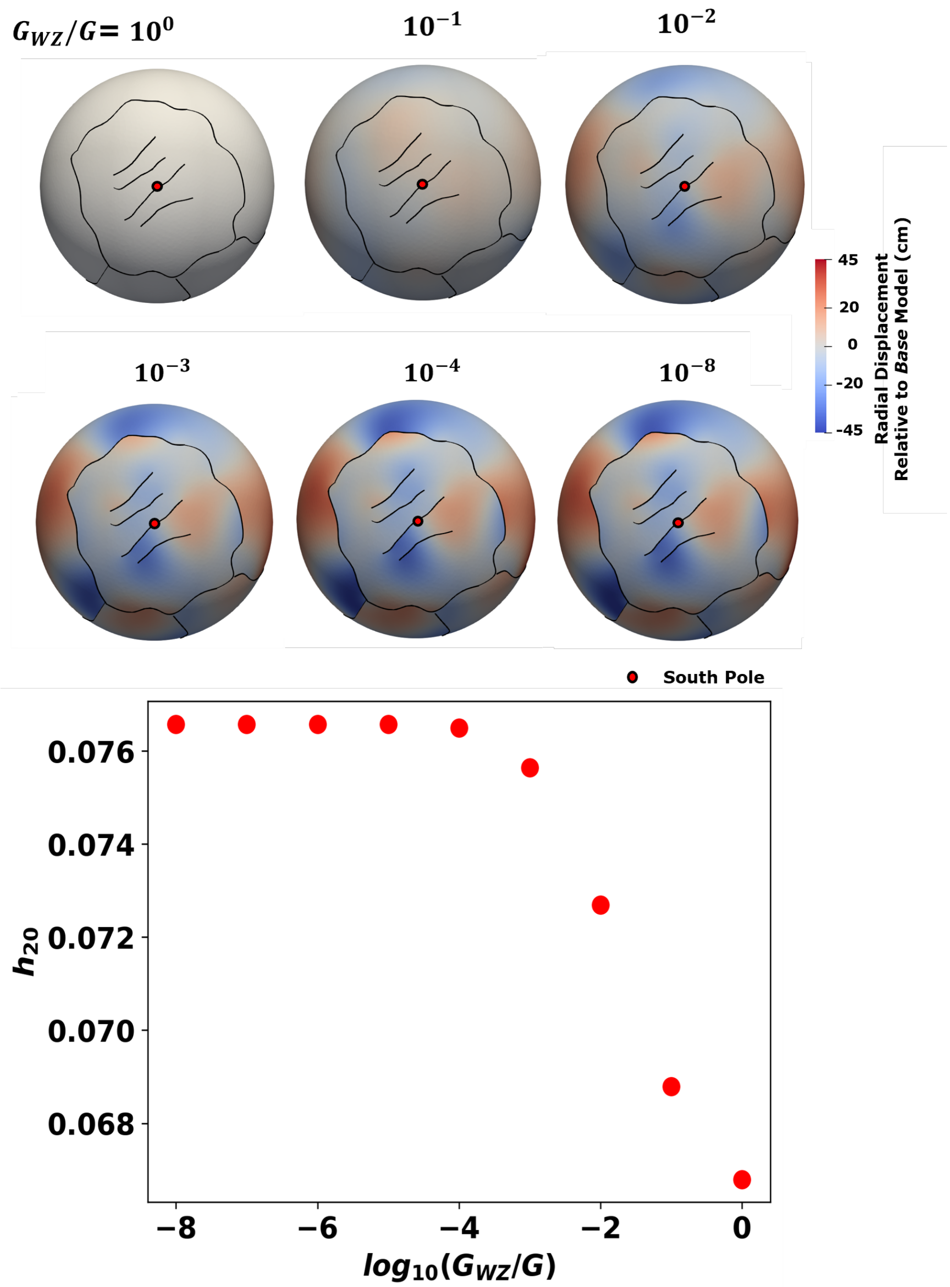

Figure 4. Results evaluated at periapse for *WZ* models ($\tilde{d}_{el}$ = 15 km) across several values of G_{WZ}. We show radial displacement fields viewed facing upwards towards the SP (top) and h_{20}^d Love number results we use as a proxy for effective model stiffness.

Letters, *43*(14). doi: 10.1002/2016GL069415

Wahr, Selvans, Z. A., Mullen, M. E., Barr, A. C., Collins, G. C., Selvans, M. M., & Pappalardo, R. T. (2009). Modeling stresses on satellites due to nonsynchronous rotation and orbital eccentricity using gravitational potential theory. *Icarus*, *200*(1). doi: 10.1016/j.icarus.2008.11.002

Wahr, Zuber, M. T., Smith, D. E., & Lunine, J. I. (2006). Tides on Europa, and the thickness of Europa's icy shell. *Journal of Geophysical Research E: Planets*, *111*(12). doi: 10.1029/2006JE002729